Biophysical Journal
Article

Biophysical Society

The Structural Basis of IKs Ion-Channel Activation: Mechanistic Insights from Molecular Simulations

Smiruthi Ramasubramanian[1] and Yoram Rudy[1,*]
[1]Department of Biomedical Engineering and Cardiac Bioelectricity and Arrhythmia Center, Washington University in St. Louis, St. Louis, Missouri

ABSTRACT Relating ion channel (iCh) structural dynamics to physiological function remains a challenge. Current experimental and computational techniques have limited ability to explore this relationship in atomistic detail over physiological timescales. A framework associating iCh structure to function is necessary for elucidating normal and disease mechanisms. We formulated a modeling schema that overcomes the limitations of current methods through applications of artificial intelligence machine learning. Using this approach, we studied molecular processes that underlie human IKs voltage-mediated gating. IKs malfunction underlies many debilitating and life-threatening diseases. Molecular components of IKs that underlie its electrophysiological function include KCNQ1 (a pore-forming tetramer) and KCNE1 (an auxiliary subunit). Simulations, using the IKs structure-function model, reproduced experimentally recorded saturation of gating-charge displacement at positive membrane voltages, two-step voltage sensor (VS) movement shown by fluorescence, iCh gating statistics, and current-voltage relationship. Mechanistic insights include the following: 1) pore energy profile determines iCh subconductance; 2) the entire protein structure, not limited to the pore, contributes to pore energy and channel subconductance; 3) interactions with KCNE1 result in two distinct VS movements, causing gating-charge saturation at positive membrane voltages and current activation delay; and 4) flexible coupling between VS and pore permits pore opening at lower VS positions, resulting in sequential gating. The new modeling approach is applicable to atomistic scale studies of other proteins on timescales of physiological function.

INTRODUCTION

A voltage-gated ion channel (iCh), in response to membrane voltage (V_m), undergoes atomistic structural changes that are stochastic in nature and underlie its physiological function as a transmembrane (TM) charge carrier. Recent advances in experimental techniques (1) provide considerable structural details that can be used to simulate atomistic structural dynamics. Relating these dynamics to the physiological function of proteins, including iCh, remains a major objective and difficult challenge in the field of biophysics. In principle, computational techniques can be used to simulate structure-based iCh function to explain its mechanism (2,3). However, even with customized hardware, simulations of 1-ms gating dynamics take months and require nonphysiological conditions, e.g., a V_m of 500 mV (4,5).Therefore, direct computation of iCh conformational changes during gating, with atomistic structural details and over a sufficiently long timescale (10s of ms), is impractical.

In this study, we introduce a methodology that utilizes machine learning (ML) for modeling iCh with structural and functional details. The method can be used to probe mechanisms that govern ionic conductance and voltage-mediated gating at sufficient atomistic resolution over physiological timescales. The protein archetype we chose is the slow delayed rectifier IKs, a human voltage-gated potassium iCh. IKs is composed of a KCNQ1 pore-forming tetramer modulated by KCNE1 segments. It plays an important role in cardiac action potential (AP) repolarization during β-adrenergic stimulation and participates in cardiac AP-rate-dependent adaptation (6,7). IKs mutations are implicated in the most common congenital long QT syndrome, Type 1, and in severe neurological disorders such as deafness and epilepsy (8). Additionally, this channel poses many structure-function molecular properties of interest, such as multiple subconductance (SC) levels, two distinct gating conformational movements, voltage sensor (VS) or S4 movement that precedes ionic current, gating-charge (GC) saturation at positive V_m, and sequential gating (9–11). The new ML-based modeling approach simulates experimental data with high accuracy and reproduces these properties; it provides mechanistic insights on

Submitted February 7, 2018, and accepted for publication April 13, 2018.
*Correspondence: rudy@wustl.edu
Editor: Eric Sobie.
https://doi.org/10.1016/j.bpj.2018.04.023

the molecular basis of iCh activation under physiological conditions.

METHODS

A short overview of simulating structural dynamics and electrophysiological function is provided below; details are included in the Supporting Materials and Methods. The energy landscape was constructed to simulate IKs structural changes in response to V_m. If done explicitly, this process requires computing the energy of all possible IKs conformations. This is an impossible task given the vast number of degrees of freedom. Previous modeling overcame these difficulties by retaining only large backbone movement with limited degrees of freedom, assuming tetrameric symmetry and reducing simulations to KCNQ1 TM segments (12–15). Here, we apply ML to simulate physiological IKs behavior at the atomistic scale, without the approximations and simplifications of previous work.

Structure to function

The initial IKs structure was constructed from experimental data using computational modeling (Fig. 1); the specifics are detailed in the Supporting Materials and Methods. Extensive de novo sampling of IKs conformational space (library: ~3,000,000 conformations) was performed without any dimension reduction, applying physiological and experimental constraints. MODELLER (16) was used to minimize energy and remove steric clashes. Selected IKs attributes (features) that alter protein energy were extracted from the library, along with the computed energy of each corresponding structure (17,18). Using these data, the ML algorithm (19) was trained to predict IKs energy of structures outside the library. With this approach, the energy landscape covered the entire IKs conformational space associated with activation. If desired, the structure for any point on the energy landscape could be retrieved. CHARMM force fields were used for energy calculations (20).

Multidimensional random walks (with Metropolis-Hastings criterion (21)) on the energy landscape at different V_m quantified the transition probability between different regions of the energy landscape. The time step of the simulated random jumps was estimated from experimentally obtained single-channel kinetic data (9) (~0.17 ms). Note that jump resolution could be as small as 10^{-12} steps, and the maximal allowed structural deviation between jumps was 1 Å. The structures visited in the random walks were clustered in two physiological dimensions of interest: Avg.S4Z (average Z position of four VS in the tetramer) and PD (the minimum pore diameter at the activation gate). Conformational jumps between structure pairs from random walks were used to construct the transition matrix of structural clusters (Supporting Materials and Methods). All simulations were conducted at room temperature (21°C), consistent with experiments. Note that PyMOL (22) was utilized for all protein visualizations.

Calculating SC using IKs pore energy

To simulate IKs function (e.g., single-channel and macroscopic current) starting from simulated structural changes during gating, each structure cluster SC was calculated. A representative structure for each cluster was used to calculate the energy profile (using particle mesh Ewald (23)) across the membrane in the pore region (Fig. 2 *A*). This pore-energy profile (energy barrier) of the representative IKs would affect the probability of an ion passing through the pore (P_{ion}). The peak of the energy barrier (located at the activation gate) was used to construct the pore-energy map (Fig. 2 *A*, *center*). This map was used to obtain parameters f (an

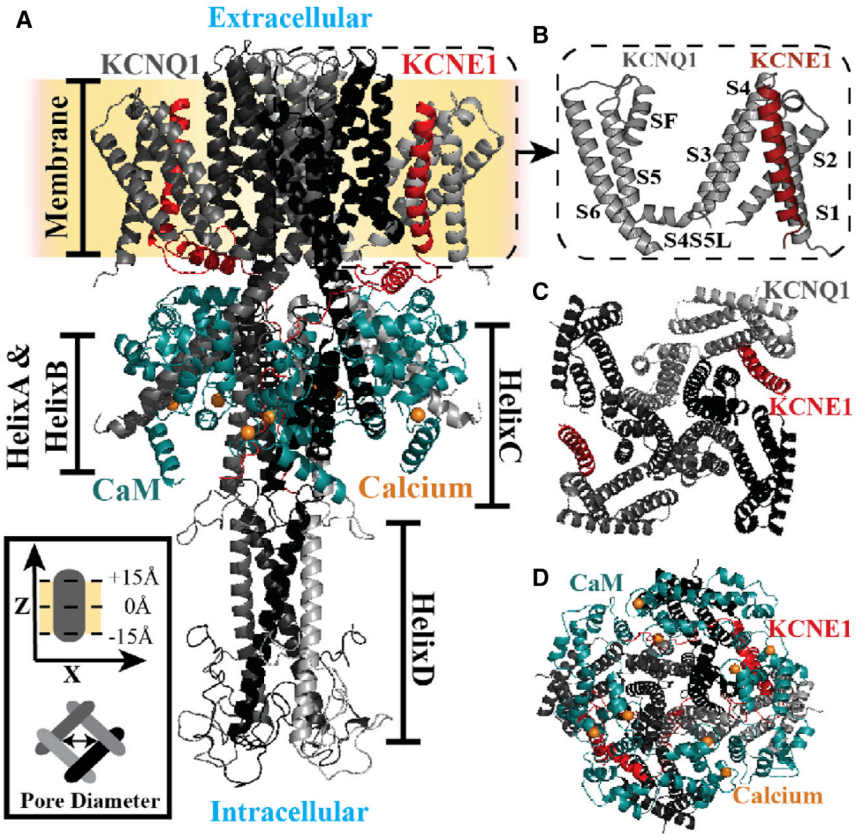

FIGURE 1 IKs structure. (*A*) A side view of initial IKs structure (KCNQ1 tetramer bound to two KCNE1) is shown. CaM is bound to HelixA&B and is proximal to the KCNE1 cytoplasmic helix. The KCNE1 intracellular segment interacts with HelixC's dimer-of-dimers, and the HelixD tetramer binds with Yotiao (protein not shown) to facilitate IKs phosphorylation. In addition, HelixC and HelixD are suggested to play a role in subunit dimerization and tetramerization, respectively (26). The inset (*bottom left*) shows the coordinate system of IKs (*gray*; *side* and *bottom* views) in the membrane (*yellow*). (*B*) An expanded view of the TM S1–S6 arrangement is shown. (*C*) A top view (without CaM and KCNQ1 C-terminus) and (*D*) bottom view of IKs are shown. The structural components and identifying symbols are color coded. S4S5L, S4-S5 linker; CaM, Apo-Calmodulin.

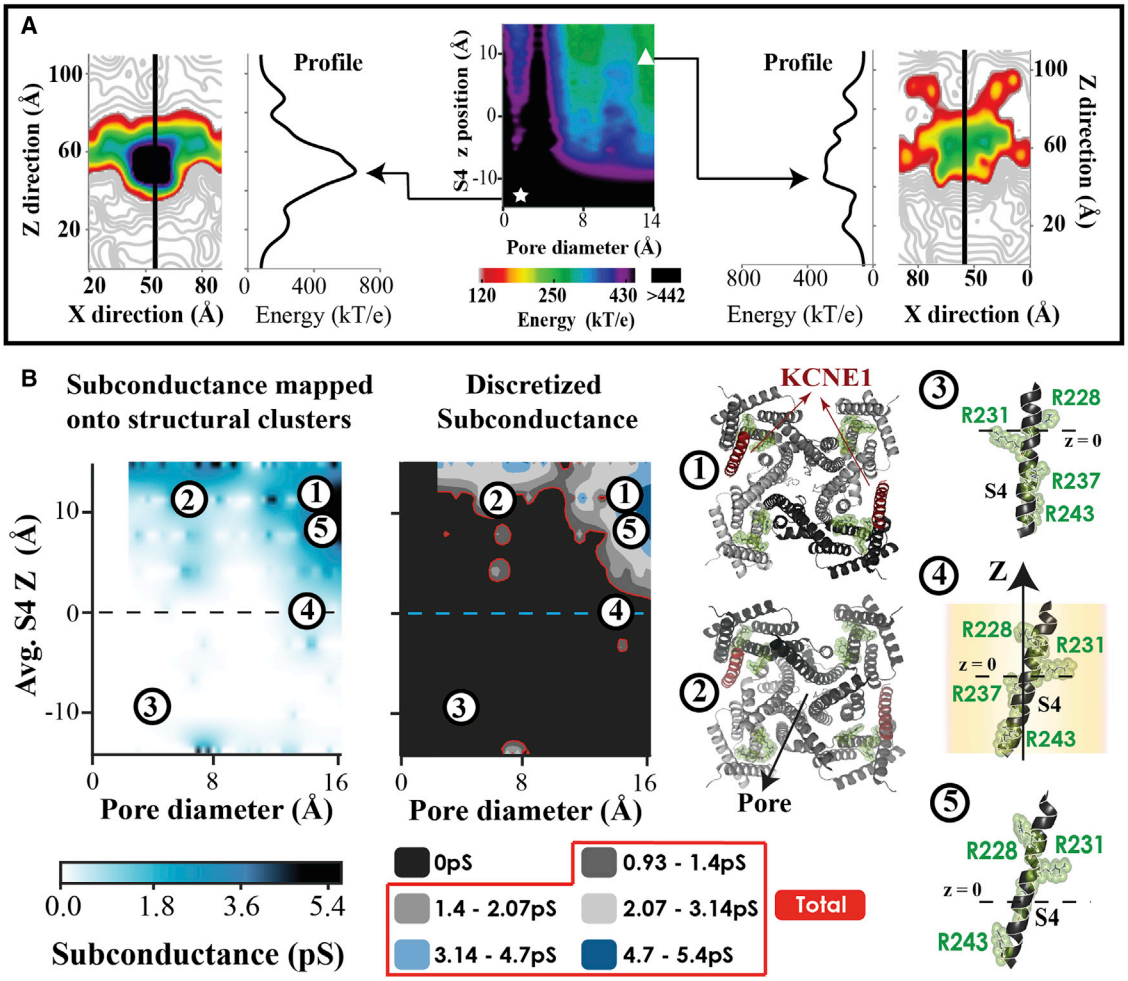

FIGURE 2 Structure-based SC computed from pore energy profile. (*A*, *center*) The largest IKs energy barrier across the pore is projected on a two-dimensional conformational cluster map (PD and Avg.S4Z position). The symbols indicate representative structures from two different clusters: low S4 *Z* position and small pore (*white star*), and high S4 and large pore (*white triangle*). Corresponding pore energy maps (*X-Z* slice) for these structures are shown together with the energy profile across the membrane along a center line (*black*). (*B*) The calculated SC values from the pore energy barrier are projected on a two-dimensional (PD and Avg.S4Z) conformational cluster map (SC map, *left*). The estimated SC are grouped into five discretized conducting levels based on experimental measurements (9) (SC map, *right*). The total conductance (*red*) is used to simulate macroscopic current and calculate single channel statistics (Supporting Materials and Methods). Protein structures in relation to SC are shown in the right panels. They depict representative pore (*bottom view*) and S4 (*side view*) structures from selected clusters on the map. Positively charged S4 residues (R228, R231, R237, R243) are identified (*green*). Numbers indicate structure locations on the SC map. Only one of four possible S4 conformations is shown.

energy-barrier-scaling constant used to account for extrinsic factors that affect ion conduction) and G_{max} (maximal conductance) of Eqs. 1 and 2, using experimental data (9,24). A Boltzmann distribution for pore energy (E) was assumed, and a self-adaptive differential evolution algorithm (25) was used to estimate SC in Eq. 2. The ionic current (I_K) (Eq. 3) was calculated based on SC and number of ion channels in cluster i (N_i), with the reversal potential (E_K):

$$P_{ion_i} = e^{(-E_i \times f)}, \tag{1}$$

$$SC_i = G_{max} \times P_{ion_i}, \tag{2}$$

and

$$I_K(t) = \sum_i SC_i \times N_i(t) \times (V_m - E_K). \tag{3}$$

G_{max} and f were estimated to be 1.9e9 S and 9.31e−2 kT/e, respectively. SC was assumed to be conformation-specific and the same at all V_m, because pore-energy profile changes due to V_m changes were negligible. A flowchart of simulation steps (Fig. S7) and details on specific gating mechanism calculations are provided in the Supporting Materials and Methods.

RESULTS

An IKs structure (Fig. 1) was constructed using available experimental data (26) and homology to Kv1.2/2.1 (Supporting Materials and Methods). Although it was not assumed that S3 and S4 move together, conformations in the library indicate that S3 moves and rotates to accommodate S4 upward movement during gating; this is expected, as the segments are tightly coupled by a short linker. The

KCNE1 TM segment also moves and rotates to accommodate S4 conformational changes.

Structural basis of SC and simulated ionic currents

The pore-energy barrier depends on IKs structure. The *Z*-profile of pore energy (Fig. 2 *A*) has a large barrier for ions to cross at the pore activation gate. However, this barrier is lower for structures with high Avg.S4Z and large PD (Fig. 2 *A*, *white triangle*). These clusters, with lower energy barriers, have a greater probability of ions passing through the pore as compared to structures with low Avg.S4Z and small PD (Fig. 2 *A*, *white star*). Consequently, they are associated with higher SC levels and greater ionic current. Fig. 2 *B* shows the calculated SC map computed from the pore-energy map (Fig. 2 *A*, *center*). Structure clusters with the lowest energy barrier (Fig. 2 *A*, *white triangle*) have large PD and high Avg.S4Z; they also have the highest estimated SC (Fig. 2 *B*; clusters 1 and 5). As such, SC is dependent on PD as previously suggested (27). Additionally, VS conformational changes and associated IKs structural changes also affect SC.

The estimated SC map (Fig. 2 *B*) was used to simulate IKs function as a current carrier. The simulated function was compared to experiments under similar conditions and voltage protocols (9) (Fig. 3, *A–E*). Simulated single-channel current traces and the macroscopic current (average of 100 such traces) showed good correspondence with experimental data (Fig. 3, *A* and *B*). SC levels, accessed during activation upon step depolarization to 60 mV from −80 mV, were equivalent to experimental measurements (Fig. 3 *C*). The simulated mean single-channel current amplitudes at different depolarized V_m were used to calculate the microscopic current-voltage (I-V) relationship; an example calculation at 60 mV is shown in Fig. 3 *D*. The I-V curve shows excellent correlation with experimental recordings (Fig. 3 *E*). Similar to experiments, simulations showed many silent single-channel traces for which IKs structural changes did not result in conducting pore conformations. Simulated single-channel latency to first opening during a step depolarization to 60 mV was 1.65 ± 0.08 s (Supporting Materials and Methods), consistent with the experimental value (1.67 ± 0.008 s, for the current amplitude of 0.5 pA). Relevant single-channel current characteristics such as total dwell time, mean open time, and first opening probability were calculated for each SC level at different V_m (Figs. S15 and S16). Simulated single-channel traces showed increased access to higher SC levels with larger depolarizing V_m.

Two distinct VS movements

Simulated structural changes, associated with VS movement during depolarization (at different V_m), were consistent with the results of fluorescence experiments (10). Analysis of 2000 IKs trajectories identified two possible VS movements at negative and positive V_m (Fig. 4). Upon depolarization, VS underwent an initial fast ~9 Å upward *Z* movement, followed by a slower ~2 Å movement (maximal Avg.S4Z translation at steady state (SS)). The rate of accompanying PD increase was slow compared to Avg.S4Z translation (Fig. 5). Simulated S4 *Z* movement preceded ionic current, consistent with experiments (10). SS occupation of structural states at −80 mV (holding potential, HP) identifies three IKs conformational clusters (HPSS clusters) likely to

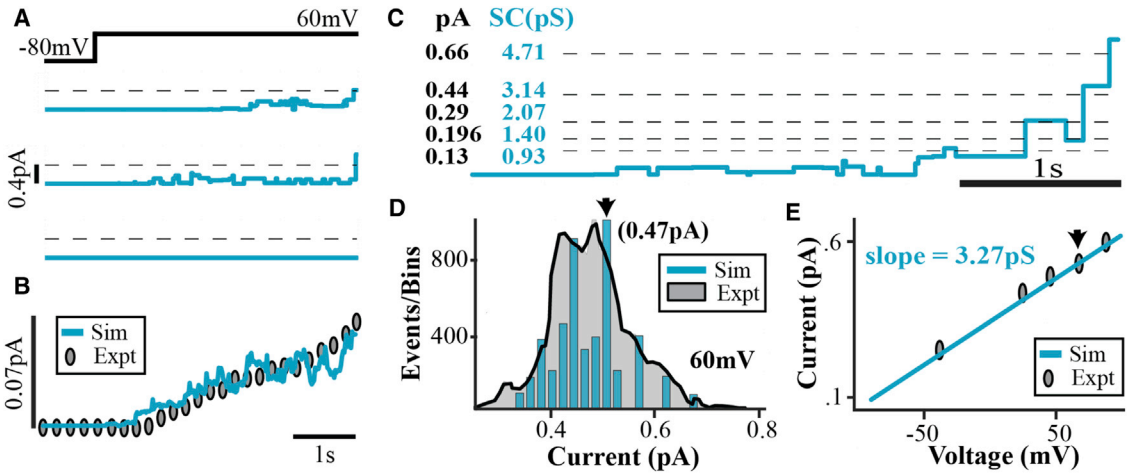

FIGURE 3 (*A*) Three simulated single-channel current traces for a step depolarization V_m from −80 to 60 mV. (*B*) The ensemble current (average of 100 traces) fits the experimental data (9). (*C*) An expanded section of a simulated single-channel trace is presented here. Experimentally identified current levels (9) (*dashed lines*, *black entries*) and SC computed from simulations (*blue entries*) are shown. (*D*) A current amplitude histogram of simulated single-channel traces at 60 mV (*blue*) and the corresponding experimental data (*shaded gray*) (9) is given. The arrow indicates the mean current amplitude histogram (0.47 pA, also indicated by the arrow in (*E*)). (*E*) Similar histograms (to (*D*)) are constructed for a range of V_m to obtain the microscopic I-V relationship (*blue line*) that fits experimental data (*symbols*) with a slope (mean conductance) of 3.27 pS (as determined experimentally (9)).

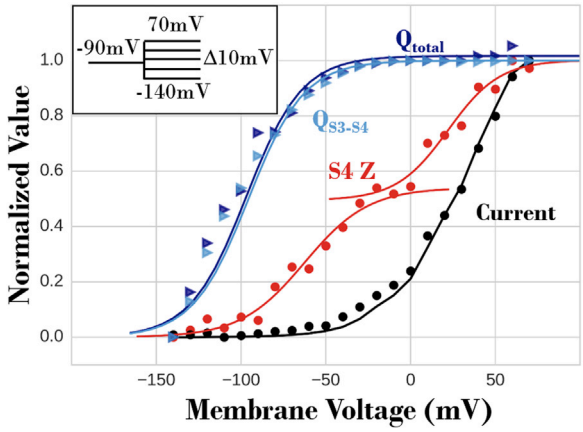

FIGURE 4 GC displacement (*blue*), S4 *Z* (*red*), and macroscopic current (*black*). Normalized simulated current (*black circles*) and the sum of tetramer S4 *Z* displacements (*red circles*) in 2000 iCh, 4 s past depolarization (for the protocol in the *inset*), are given. The black line represents experimental data (24). The S4 *Z* data are fitted with two sigmoidal curves at negative and positive V_m, representing the I and II movements of S4, respectively. At positive V_m, an increasing fraction of S4 in the 2000 iCh transitions to the II movement. GC displacement associated with one representative iCh S4 *Z* transition is calculated based on two selections: the entire IKs (Q_{total}, *dark blue*) and S3-S4 segments only (Q_{S3-S4}, *light blue*) at different V_m. The GC data are fitted with a single sigmoid (*light* and *dark blue traces*), analogous to the S4 *Z* data at negative V_m.

transition to conducting conformations upon depolarization (Fig. 5, *right-top*, *blue*, *green*, *pink symbols*). Three likely pathways between HPSS clusters and high SC cluster (Fig. 5, *right-top*, *black symbol*) were ascertained for 60 mV step depolarization. The temporal probability of each pathway (Fig. 5, *right-middle*) showed that conformations with large pore at −80 mV transition faster to high SC conformations (large PD, high Avg.S4Z) than conformations with a smaller pore. Fig. 6 provides a summary and schematic representation of S4 and pore conformational changes during activation.

Important residue-pair interactions that affected VS conformational changes were identified by calculating their contribution to IKs structural energy (Fig. S17). There are two S4 positions relative to KCNE1, proximal and distal (Figs. 1 *C* and S17). Proximal S4 charged residues interacted strongly with charged residues at the bottom of the KCNE1 segment (Fig. S17 *C*). In contrast, two distal S4 charged residues were only weakly influenced by KCNE1 (Fig. S17 *B*). These differences resulted in two types of VS *Z* movement of proximal S4 and distal S4, respectively. Residue-interaction-energy computations (Fig. S17) show stabilization of distal S4 at *Z* position 1.44 Å and of proximal S4 at 1.44 and 2.88 Å. In addition, proximal S4 shows strong stabilization at −6.75 and −4.44 Å and increasing stabilization between 0.33 and 2.88 Å. These different stabilization profiles (Fig. S17, *B* and *C*; *bottom panel*) suggest that distal S4 undergoes a single fast *Z* movement to its stabilized high *Z* position, whereas proximal S4 experiences two movements—a slower *Z* translation to about −2.78 Å, followed by a faster upward *Z* movement to ∼3 Å. It follows that distal S4 contributes mostly to the initial fast and large *Z* translation (to ∼1 Å), and proximal S4 is responsible for the additional slower S4 *Z* movement (to ∼3 Å) at positive V_m, resulting in more conformations transitioning to high SC clusters.

GC saturation and sequential gating

The model also replicated the experimentally observed saturation of GC displacement at positive V_m (Fig. 4). This property is the result of the two aforementioned VS *Z* movements—at negative V_m, the VS underwent a fast and large *Z* translation with large charge displacement, and at positive V_m it experienced an additional slow and small *Z* translation (Fig. 6) that contributed very little to GC displacement. GC calculations with only S3–S4 segments (Q_{S3-S4}) and with the entire protein (Q_{total}) showed that S3–S4 movement contributes most to GC displacement. Using alternative structural clustering (Supporting Materials and Methods), all possible combinations of S4 *Z* movements in the tetramer were suppressed, and macroscopic current (2000 IKs channels) at the end of 4-s step depolarization was recorded (Fig. 7). Ten simulations were conducted for each combination of immobilized S4, and the resulting currents were normalized to control (IKs current with all four S4 mobile). If S4 movements were cooperative and required concerted transitions during gating, then the immobilization of S4 would have resulted in zero current. However, Fig. 7 shows that current decreases linearly with an increased number of immobilized S4, consistent with experimental data (11). This linearity confirms independent S4 movement and shows that each S4 contributes incrementally to IKs gating.

SC validation

In addition to computing SC from simulated pore energy (Fig. 2 *B*), SC was estimated from fitting experimental data (Fig. S18). The estimated SC map was used to simulate macroscopic current, microscopic current, and I-V relationships (Fig. S18, *A–D*) with high accuracy relative to experiments (9,24); the SC map from experimental data (Fig. 18 *E*) was extremely similar to the SC map calculated from pore energy (Fig. 2 *B*), with analogous locations of high SC clusters and nonconducting clusters.

DISCUSSION

Experimental techniques that visualize atomistic structural dynamics (28) are difficult to utilize with large IKs proteins, because they contain multiple domains with flexible regions. Molecular dynamics simulations provide valuable data on a possible structural pathway between two known iCh conformations (endpoints) on the millisecond

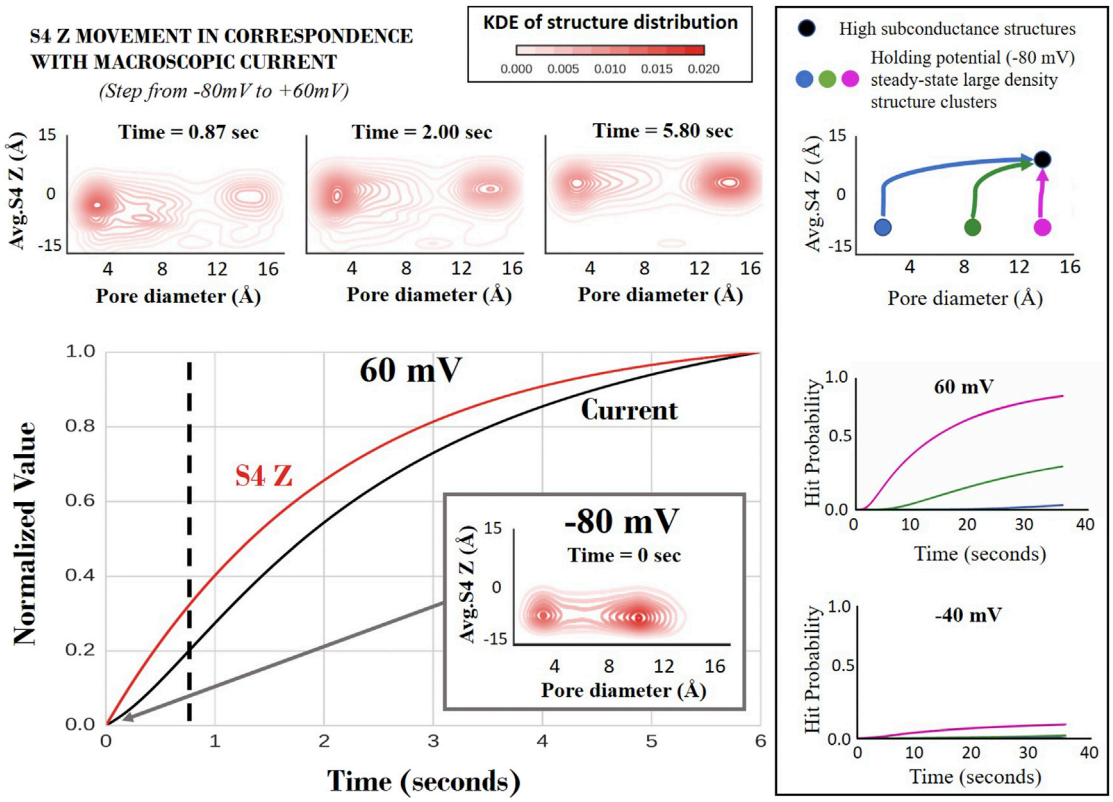

FIGURE 5 Two movements of the voltage sensor and pore. (*Center*) The normalized S4 *Z* movement and macroscopic current (2000 ion channels), calculated for a depolarizing potential to 60 mV from a holding potential of −80 mV, show that the S4 movement in the *Z* direction precedes ion conduction through the pore. The dashed line divides approximately the two time courses of major conformational changes between structure clusters shown in the right panel. (*Top*) The KDEs calculated based on the temporal occupancy of the structure clusters are shown at the top for three different times. Comparing the structure-cluster KDE at −80 mV holding potential (*center panel* (*inset*)) and 0.87 s after 60 mV depolarization, it can be seen that the initial movement of S4 in the *Z*-direction (∼9 Å) is fast. As time progresses (at 2 and 5.8 s), the S4 *Z* moves slower to a slightly higher *Z* position (∼1.4 Å, at 6 s) with high conductance. The pore opening from a small to a large pore diameter is also much slower than the initial S4 movement. (*Right*) The top panel identifies major cluster structures occupied at a holding potential of −80 mV (*pink*, *green*, and *blue filled circles*). They correspond to the KDE map at −80 mV (*center panel*), except the pink clusters do not show on the map scale. The colored arrows mark the most probable trajectories of the structures to the high SC clusters (*black filled circle*) during application of a depolarizing potential. The middle and bottom panels show the time progression of the probability of these trajectories (*color coded*) for two different membrane potentials, +60 mV (*middle*) and −40 mV (*bottom*).

timescale. Because single-channel dynamics are stochastic, extensive IKs structural changes occur between closed and open states as a function of V_m and time, ensuing in multiple transition pathways over a millisecond-to-second timescale. Therefore, multiple endpoints molecular dynamics computations are not viable on a physiological timescale (5,29). Previous structure-based functional models did not account for SCs because a single-conductance concerted or allosteric constraint was assumed to simulate current (12–15). Knowledge of an experimentally resolved static iCh structure, although insufficient to decipher global structural dynamics, provides a plethora of information (e.g., secondary structure propensities, flexible regions, connectivity, etc.) to build a library of possible gating conformations at the required atomistic resolution (Methods and Supporting Materials and Methods). Many of our library IKs conformations (sans KCNE1) were found with small deviations from the recently published electron cryo-microscopy (cryo-EM) KCNQ1 structure (Fig. S11).

The ML algorithm (19) used to construct the multidimensional protein energy landscape converged and was able to predict IKs structural energy with negligible error (Supporting Materials and Methods). This approach circumvented the impossible computation of constructing all possible IKs structures. To correlate the simulated structural transitions to experimentally measured ionic current, the partition function of the computed energy landscape was obtained from IKs single-channel kinetics (9). Library IKs structural energy shows that electrostatic energy contributes overwhelmingly to the total energy (Supporting Materials and Methods; Figs. S12 and S13). As a result, changes in IKs energy due to V_m can be adequately represented by changes in electrostatic energy. The simulated structural and functional changes were validated using independent experiments, other than those used for parameter estimations; the IKs model reproduced the recordings of ensemble structural changes, ionic current characteristics, and I-V relationships (10,11,24).

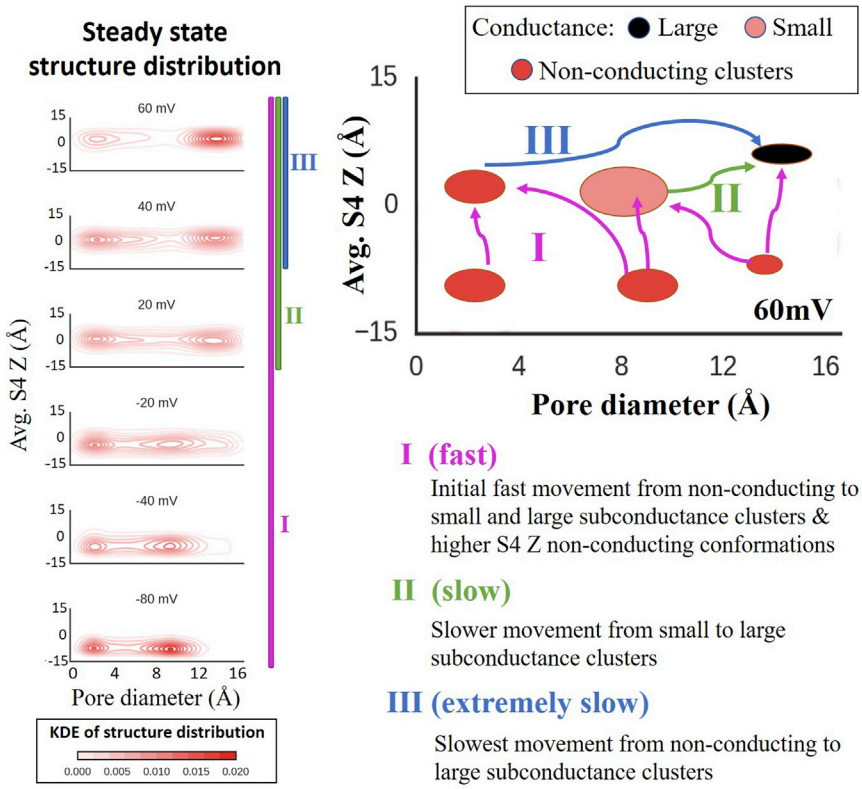

FIGURE 6 Fast and slow movements of the S4 in *Z* direction and pore opening. (*Left*) The steady-state structure cluster KDE for the indicated V_m when depolarized from the holding potential of −80 mV is shown. These panels represent transitional structure distributions when a step voltage of 60 mV is applied from a holding potential of −80 mV. The comparison of the temporal KDE plots (Fig. 5, *top*) with the steady-state KDE (*left*) indicates that at negative V_m, only the first fast transition (I) occurred, whereas at positive V_m, the first transition followed by a slower second transition (II) was observed. The first transition captures the major movement of the S4 in the *Z* direction, after which the second transition only shows a slight increase in the S4 *Z* (∼1.4 Å) and is consistent with the gating charge calculations shown in Fig. 4. The slowest transition (III) contributes very little to the current and conformational changes observed in the simulation time course. (*Right*) Cartoon schema of the fast, slow, and extremely slow conformational changes. The pink arrows represent the initial fast conformational transition because of S4 movement in the *Z* direction, whereas the green arrow shows the slower transition from medium to large pore and the further small S4 *Z* movement. The blue arrow represents the extremely slow transition from a very small pore to a large pore. Note that the observed transitions are not sequential and happen simultaneously.

IKs structure-based SC determination

IKs structural changes in response to V_m depolarization were simulated, and the corresponding function (ionic current) was calculated by associating a pore conductance to a structure cluster. Gating conformations with S4 at higher *Z* have lower energy barriers at the pore activation gate. This is because the repulsive electrostatic field in the pore, influenced by the four positively charged S4 segments (tetramer), is mitigated by the shielding effect of the surrounding protein segments and water at higher S4 *Z* positions. Therefore, conformations with low or high S4 *Z* positions have low or high SC levels, respectively. In addition, SC levels are also affected by PD.

The pore-energy profile was computed in the absence of explicit K^+ ions in the pore. This permitted us to calculate SC as an intrinsic property of IKs, independent of extrinsic factors that affect ion conduction such as number, location, and hydration characteristics of pore ions. Therefore, SC computations are based solely on the IKs molecular structure and its propensity to allow ionic conduction. With these properties, the model correlates structural changes to functional observations and replicates experimentally observed IKs characteristics, including five discrete SC levels (between 0.13 and 0.66 pS (9)).

Analysis of early IKs single channel recordings showed a four-times-larger conductance as compared to KCNQ1 (24,30). It also displayed a strong Cole-Moore effect, i.e., activated VS did not result in immediate current. It was suggested that this difference could be due to KCNQ1's ability to access multiple SC states, whereas IKs could only access the largest SC state during activation (31). However, IKs and KCNQ1 do not have access to the same SC states during VS activation. In the absence of KCNE1, the structure-based SC map of KCNQ1 changes significantly. Without the mitigating effect of negatively charged KCNE1 residues, the energy barrier across the KCNQ1 pore is larger for high-S4-*Z* and wide-pore KCNQ1 conformations. In the absence of KCNE1, we anticipate that KCNQ1 S4 will behave similarly to distal S4 of IKs and will not have the II S4 movement (that allows access to larger SC states; Fig. 6). With this information, we envision that both KCNQ1 and IKs conduct ionic current at multiple SC levels, and we further predict that the KCNQ1 SC range will be three to four times smaller than that of IKs. It follows that, for every addition of KCNE1 to KCNQ1, larger SC states will be accessible by the iCh.

S4 movement precedes ion conduction through the pore

Fluorescence experiments provide data on S4 movement during channel gating. However, this technique cannot quantify the exact S4 movement. Also, depending on the probe utilized, fluorescence intensity measurements can

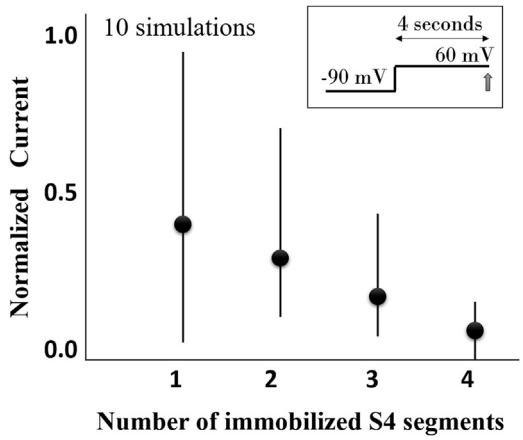

FIGURE 7 Sequential movement of S4 governs IKs gating. Using an alternative structure clustering method, an increasing number of S4 segments were prevented from moving upward during depolarization to 60 mV. The resulting current is measured 4 s postdepolarization (protocol in the *inset*). The plot shows a linear decrease of current with increasing number of immobilized S4 segments. Ten simulations were performed for each combination of S4 suppression. For example, two immobilized S4 segments could either be on adjacent or opposite sides of the tetramer. The 10 simulations for each of the possible S4 suppression combinations yielded the current mean (*filled circle*) and the minimum and maximum (error bars) of the plotted values. The results were normalized to the control (simulation of current without S4 movement suppression). The large variance is due to dissimilarity in ionic current reduction depending on whether proximal or distal S4 was immobilized.

vary. Therefore, we assumed that S4 *Z* translation across the membrane contributes most to changes in fluorescence, with smaller effects due to rotation or *X*, *Y* translation. In support of this assumption, the computed sum of four S4 *Z* displacements (Fig. 4) was consistent with experimental fluorescence data (10). As in experiments, simulated macroscopic current showed slower rise relative to S4 *Z*, indicating that S4 *Z* movement leads pore ion conduction (Figs. 4 and 5). Simulations show that initial movements of S4 and pore, because of depolarizing V_m, result in conformations with low or nonconducting SC. Therefore, little to no current is observed at first. With time, as IKs transitions to higher S4 Z and larger PD, higher SC levels are accessed, resulting in a larger current.

Other IKs fluorescence experiments also show two distinct fluorescence-voltage components (F1 and F2): F1 representing the large and fast IKs movements at negative V_m and F2 the smaller and slower component measured at positive V_m, respectively (31,32). These experiments also showed that the second structural IKs movement (represented by F2) correlated with significant increase in current. Therefore, in agreement with a concerted gating model, it was proposed that F1 and F2 components represented S4 activation and pore opening, respectively (7,10). However, this IKs gating model could not account for SCs reported by IKs single-channel recordings and had to be modified to include conductance levels for different numbers of activated S4 in the tetramer (9). Our model is consistent with the latter premise that with increasing number of activated VS, IKs can access larger SC states. However, our model does not reproduce the rapid transitions of IKs from large SC to nonconducting states. We believe that these transitions are caused by extrinsic SC factors that are not represented in this model, e.g., number and location of ions in the pore, ion hydration, van der Waals interactions between ions, water and pore residues, presence of nonpotassium ions in the pore, etc.

IKs conformational trajectories after depolarization

Fig. 5 (*right*) identifies important structural clusters and major conformational pathways (groups of trajectories) upon depolarization from −80 to 60 mV and −40 mV. The pink pathway encompasses mostly S4 *Z* translations, and the green and blue pathways include pore expansion. These pathways were identified by analyzing trajectories from each starting HPSS clusters to high SC clusters. Hit probabilities (transition probability between identified clusters) show that very few deeply closed conformations (small pore and low S4 *Z*) transition to high SC clusters upon depolarization (*blue*). Interestingly, 78% of total structures occupy this small-pore, low-S4-*Z* cluster at −80 mV. Very few IKs channels occupy the pink cluster and thus contribute very little to current upon depolarization. Nevertheless, this trajectory is responsible for the initial current increase. Approximately 18% of conformations occupy the green cluster and contribute to current rise later in time. As expected, the probability of transitioning to high SC clusters is smaller at −40 mV than at 60 mV. The pathways used to calculate hit probabilities are the major structural transitions that contribute to ionic current during IKs activation. As a model-based inference, we suggest that these pathways are closely related to experimentally detected current activation time constants, i.e., the fast and slow time constants correspond with pink and green pathways in Fig. 5, respectively.

S4 movement and pore opening

Similar to S4 *Z* upward movement, the pore follows an independent time course of opening. Hit probabilities (Fig. 5, *right*) show that the pathway of mostly S4 upward movement (*pink*) was much more probable than other pathways (*green* and *blue*). The pathway that required the largest PD increase (*blue*) to reach high SC states was least probable. Thus, initial Avg.S4Z transition (from −10 to ∼1 Å) was much faster than the second Avg.S4Z transition (from ∼1 to 3 Å), which in turn was faster than pore opening. A cartoon in Fig. 6 (*right*) explains these dynamics further.

Using kernel density estimation (KDE) of occupied structure clusters at SS for a range of V_m between −80 and 60 mV

helped identify important cluster groups that were visited upon depolarization (Fig. 6, *left*). Temporal KDE data (Fig. 5, *top*) show that conformations experiencing step depolarization to negative V_m undergo only the first fast transition (I), in which the dynamics are mostly determined by upward S4 *Z* translation (from −8 to ∼1 Å). For positive depolarization to V_m, conformations initially experience the first transition, followed by a second slower transition (II) of small S4 *Z* movement (from ∼1 to 3 Å) and medium to large PD increase, consistent with experimental data (10). The VS two-step transitions correlate with the fast (I) and slow (II) transitions of S4 (Fig. 4). Ionic current follows S4 movement with a delay because pore opening is slow compared to S4 *Z* transitions.

The third, much slower transition (III), from very small to large pore, involves small S4 *Z* movement (from ∼1 to 3 Å) that occurs at positive V_m and takes a much longer time. Consequently, IKs channels take a very long time to reach SS. This provides a likely explanation for the experimentally observed IKs current increase over very long times postdepolarization.

For one iCh, I contributes most to GC displacement. II, at positive V_m, involves a very small S4 *Z* translation and therefore contributes much less to GC displacement. As V_m increases, more iCh transition to conformations with higher S4 *Z*, as reflected in the sum shown in Fig. 4 (*red*). However, for one iCh, the S4 *Z* movement is small and contributes minimally to GC, which exhibits saturation (Fig. 4, *blue*).

Our structurally based model of IKs shows similar characteristics to the Zaydman-Cui kinetic (Markov) IKs model (32); the movement "I" (resting to intermediate state transitions) confers little to no current in both models. It follows that our structure-based model can be correlated to the Zaydman-Cui kinetic model that represents simplified transitions from resting to intermediate and intermediate to activated states. The correspondence requires a small modification to the Zaydman–Cui model of IKs; instead of suppressing transitions from intermediate-closed to intermediate-open states in the presence of KCNE1, the intermediate-open and activated-open states could be associated with very small and large conductances, respectively. This adjustment will enable transitions between intermediate-open and activated-open states, vital for IKs activation in our structure-based model. With this modification, the resting, intermediate and activated kinetic states can be associated with Avg.S4 Z conformations less than −5 Å, between −5 and ∼1.2 Å and greater than ∼1.2 Å, respectively. Also, we suggest that the Zaydman-Cui model of KCNQ1 could be modified with similar adjustments, but with a reduced difference between intermediate-open and activated-open conductances to account for its smaller SC range. The Zaydman-Cui model suggests that the functional VS-pore coupling is reduced in IKs relative to KCNQ1. Our structure-based model of IKs supports this supposition, as transitions to intermediate conformations result in extremely small current, and transitions to activated states are required for substantial increase in current.

Residue interactions that govern S4 *Z* movement

IKs conformational changes, in the presence of V_m, depend largely on the environment of charged S4 residues. Fig. S17 *A* shows a cartoon depicting S4 charged residues as well as the surrounding charged residues in the VS domain (S1–S4) and KCNE1 TM segment. Interaction strength between residue pairs and contribution of individual charged S4 residues to protein stabilization show that proximal and distal S4 undergo two types of movement based on their proximity to KCNE1. Distal S4 is likely to move upward faster than proximal S4 upon depolarization (Fig. S17 *B*) because strong interactions between proximal S4 and KCNE1 slow S4 transitions from low to high *Z* positions, resulting in slow activation (Fig. 17 *C*). Charged KCNE1 residues (R67, K69, K70, and E72) interact strongly with proximal S4 residues and have weaker interactions with distal S4 residues. These KCNE1 residues contribute most to proximal S4 stabilization at low *Z* through their interactions with R243 and D242 residues. Distal S4 is likely to be stabilized at ∼1 Å after depolarization and is unlikely to transition further in the *Z* direction. However, proximal S4 (although slower), can transition to higher S4 *Z* positions (∼3 Å). Ensemble VS movement has an initial large transition (fast) followed by a smaller *Z* transition (slow). The second ensemble S4 movement, observed at positive V_m (Fig. 4), is likely the result of proximal S4 transitioning from intermediate-to-high *Z* positions. The first ensemble S4 movement is possibly a combination of fast distal S4 (low-to-high) and slow proximal S4 (low-to-intermediate) *Z* transitions. In both proximal and distal S4, R228 plays an important role in stabilizing S4 at high *Z* positions.

Sequential gating

The simulations show that macroscopic current increases linearly with increasing number of moving S4 segments (Fig. 7). This is because IKs SC depends on all four S4 and pore conformations. High SC conformations are only accessible when all four S4 move to high *Z* positions with large PD. Nonetheless, small and intermediate SC conformations are accessible at low S4 *Z* with medium-to-large PD. The IKs pore is not tightly coupled to S4 *Z* movement because of the flexible S4-S4S5L three-residue segment (QGG; an additional ∼25° flexibility compared to Kv1.2/2.1 (33)). Thus, IKs pore openings (with small or intermediate SC conformations) are possible at lower S4 *Z* conformations. Large pore opening is most probable with all four S4 at high *Z*. Structurally, the pore can open (increase in diameter) at low-to-medium S4 *Z* positions, but the model IKs does not present with significant current until S4 *Z* reaches

relatively high positions. Consequently, from a model-based inference, we suggest that IKs gating is structurally allosteric but functionally concerted.

CONCLUSIONS

The methodology presented here is a computational framework for studying, through simulations, the atomistic interactions and dynamics of a protein that govern its biological function. The framework is applicable to most proteins and is a powerful tool for understanding protein behavior. This methodology can also be applied to study the effects of mutations, ligands, and drugs. Additionally, IKs structural and functional changes during an AP can be examined (34,35).

The structural model (Fig. 1) is not based on the recently published cryo-EM data of KCNQ1 structure bound to calmodulin (CaM) (33). This cryo-EM structure presents close homology to Kv1.2/2.1 TM segments and is very similar to the initial IKs structure in our library, with some differences in the intracellular domain. In particular, our model presents a different S6-HelixA attachment and number (three in Cryo-EM versus two in model) of Ca ions bound to CaM. The framework presented here allows incorporating these features into future structural libraries for evaluation of their effects on gating. We estimate that contribution to IKs energy will be minimal, as CaM is in the water/ion medium. Also, the presence of KCNE1 in our structures (but not in the cryo-EM structure) is an important feature of human IKs, as it could restrict pore opening.

The presented model uses implicit dielectrics to represent membrane and water/ion surfaces. Thus, it is possible that important van der Waals interactions between the protein and membrane that affect gating could have been underestimated. However, given that IKs C-terminus extends over 60 Å, explicit calculations would slow the computation 200-fold. With future advances in computational hardware and algorithms, it will likely be possible to incorporate an all-atom energy calculation as part of the gating model. In this study, protein dynamics was coarse-grained (by clustering structures) but was sufficiently fine to replicate all experimental data. The resolution can be tuned, based on study requirements, by increasing the number of structure clusters and random walks.

SUPPORTING MATERIAL

Supporting Materials and Methods. Supporting Results, and eighteen figures are available at http://www.biophysj.org/biophysj/supplemental/S0006-3495(18)30469-7.

AUTHOR CONTRIBUTIONS

S.R. performed the simulations and analyzed data. Y.R. supervised the project and analyzed data. Both authors conceived the project and wrote the manuscript.

ACKNOWLEDGMENTS

The authors are grateful to Prof. Bernard Attali, Tel Aviv University, for providing experimental data.

This study was supported by National Institutes of Health–National Heart, Lung, and Blood Institute grants R01-HL-033343 and R01-HL-049054 (to Y.R.). Y.R. is the Fred Saigh Distinguished Professor at Washington University. Computations were performed using facilities in the Rudy Lab and Washington University Center for High-Performance Computing, which is partially supported by National Center for Research Resources grant 1S10RR022984-01A1.

REFERENCES

1. Murata, K., and M. Wolf. 2018. Cryo-electron microscopy for structural analysis of dynamic biological macromolecules. *Biochim. Biophys. Acta.* 1862:324–334.
2. Rudy, Y., and J. R. Silva. 2006. Computational biology in the study of cardiac ion channels and cell electrophysiology. *Q. Rev. Biophys.* 39:57–116.
3. Rudy, Y. 2012. Mathematical modeling of complex biological systems: From genes and molecules to organs and organisms: heart. *In* Comprehensive Biophysics. E. H. Egelman, ed. Elsevier, pp. 268–327.
4. Jensen, M. O., D. W. Borhani, …, D. E. Shaw. 2010. Principles of conduction and hydrophobic gating in K+ channels. *Proc. Natl. Acad. Sci. USA.* 107:5833–5838.
5. Silva, J. R. 2018. How to connect cardiac excitation to the atomic interactions of ion channels. *Biophys. J.* 114:259–266.
6. Banyasz, T., Z. Jian, …, Y. Chen-Izu. 2014. Beta-adrenergic stimulation reverses the I Kr-I Ks dominant pattern during cardiac action potential. *Pflugers Arch.* 466:2067–2076.
7. Silva, J., and Y. Rudy. 2005. Subunit interaction determines IKs participation in cardiac repolarization and repolarization reserve. *Circulation.* 112:1384–1391.
8. Omichi, C., Y. Momose, and S. Kitahara. 2010. Congenital long QT syndrome presenting with a history of epilepsy: misdiagnosis or relationship between channelopathies of the heart and brain? *Epilepsia.* 51:289–292.
9. Werry, D., J. Eldstrom, …, D. Fedida. 2013. Single-channel basis for the slow activation of the repolarizing cardiac potassium current, IKs. *Proc. Natl. Acad. Sci. USA.* 110:E996–E1005.
10. Barro-Soria, R., S. Rebolledo, …, H. P. Larsson. 2014. KCNE1 divides the voltage sensor movement in KCNQ1/KCNE1 channels into two steps. *Nat. Commun.* 5:3750.
11. Meisel, E., M. Dvir, …, B. Attali. 2012. KCNQ1 channels do not undergo concerted but sequential gating transitions in both the absence and the presence of KCNE1 protein. *J. Biol. Chem.* 287: 34212–34224.
12. Nekouzadeh, A., and Y. Rudy. 2016. Conformational changes of an ion-channel during gating and emerging electrophysiologic properties: application of a computational approach to cardiac Kv7.1. *Prog. Biophys. Mol. Biol.* 120:18–27.
13. Nekouzadeh, A., and Y. Rudy. 2011. Continuum molecular simulation of large conformational changes during ion–channel gating. *PLoS One.* 6:e20186.
14. Nekouzadeh, A., J. R. Silva, and Y. Rudy. 2008. Modeling subunit cooperativity in opening of tetrameric ion channels. *Biophys. J.* 95:3510–3520.
15. Silva, J. R., H. Pan, …, Y. Rudy. 2009. A multiscale model linking ion-channel molecular dynamics and electrostatics to the cardiac action potential. *Proc. Natl. Acad. Sci. USA.* 106:11102–11106.
16. Webb, B., and A. Sali. 2014. Protein structure modeling with MODELLER. *Methods Mol. Biol.* 1137:1–15.

17. Baker, N. A., D. Sept, …, J. A. McCammon. 2001. Electrostatics of nanosystems: application to microtubules and the ribosome. *Proc. Natl. Acad. Sci. USA.* 98:10037–10041.

18. Callenberg, K. M., O. P. Choudhary, …, M. Grabe. 2010. APBSmem: a graphical interface for electrostatic calculations at the membrane. *PLoS One.* 5:e12722.

19. Buitinck, L., G. Louppe, …, G. Varoquaux. 2013. API design for machine learning software: experiences from the scikit-learn project. *arXiv*:1309.0238, https://arxiv.org/abs/1309.0238.

20. Best, R. B., X. Zhu, …, A. D. MacKerell. 2012. Optimization of the additive CHARMM all-atom protein force field targeting improved sampling of the backbone φ, ψ and side-chain χ1 and χ2 dihedral angles. *J. Chem. Theory Comput.* 8:3257–3273.

21. Hastings, W. K. 1970. Monte Carlo sampling methods using Markov chains and their applications. *Biometrika.* 57:97–109.

22. LLC Schrödinger. 2015. The PyMOL Molecular Graphics System, Version 1.8..

23. Darden, T., D. York, and L. Pedersen. 1993. Particle mesh Ewald: an N.log(N) method for Ewald sums in large systems. *J. Chem. Phys.* 98:10089–10092.

24. Yang, Y., and F. J. Sigworth. 1998. Single-channel properties of IKs potassium channels. *J. Gen. Physiol.* 112:665–678.

25. Biscani, F., D. Izzo, and M. Maertens. 2017. esa/pagmo2: pagmo 2.5. In Zenodo.

26. Haitin, Y., and B. Attali. 2008. The C-terminus of Kv7 channels: a multifunctional module. *J. Physiol.* 586:1803–1810.

27. Chapman, M. L., and A. M. VanDongen. 2005. K channel subconductance levels result from heteromeric pore conformations. *J. Gen. Physiol.* 126:87–103.

28. Nango, E., A. Royant, …, S. Iwata. 2016. A three-dimensional movie of structural changes in bacteriorhodopsin. *Science.* 354 (6319):1552–1557.

29. Howard, R. J., V. Carnevale, …, B. S. Rothberg. 2018. Permeating disciplines: overcoming barriers between molecular simulations and classical structure-function approaches in biological ion transport. *Biochim. Biophys. Acta.* 1860 (4):927–942.

30. Sesti, F., and S. A. Goldstein. 1998. Single-channel characteristics of wild-type IKs channels and channels formed with two minK mutants that cause long QT syndrome. *J. Gen. Physiol.* 112:651–663.

31. Osteen, J. D., C. Gonzalez, …, R. S. Kass. 2010. KCNE1 alters the voltage sensor movements necessary to open the KCNQ1 channel gate. *Proc. Natl. Acad. Sci. USA.* 107:22710–22715.

32. Zaydman, M. A., M. A. Kasimova, …, J. Cui. 2014. Domain-domain interactions determine the gating, permeation, pharmacology, and subunit modulation of the IKs ion channel. *eLife.* 3:e03606.

33. Sun, J., and R. MacKinnon. 2017. Cryo-EM structure of a KCNQ1/CaM complex reveals insights into congenital long QT syndrome. *Cell.* 169:1042–1050.e9.

34. O'Hara, T., L. Virág, …, Y. Rudy. 2011. Simulation of the undiseased human cardiac ventricular action potential: model formulation and experimental validation. *PLoS Comput Biol.* 7:e1002061.

35. Clancy, C. E., and Y. Rudy. 1999. Linking a genetic defect to its cellular phenotype in a cardiac arrhythmia. *Nature.* 400:566–569.

Biophysical Journal, Volume *114*

Supplemental Information

The Structural Basis of IKs Ion-Channel Activation: Mechanistic Insights from Molecular Simulations

Smiruthi Ramasubramanian and Yoram Rudy

Supplement

The Structural Basis of IKs Ion-Channel Activation: Mechanistic Insights from Molecular Simulations

By

Smiruthi Ramasubramanian and Yoram Rudy

Table of Contents

Section 1

Structure

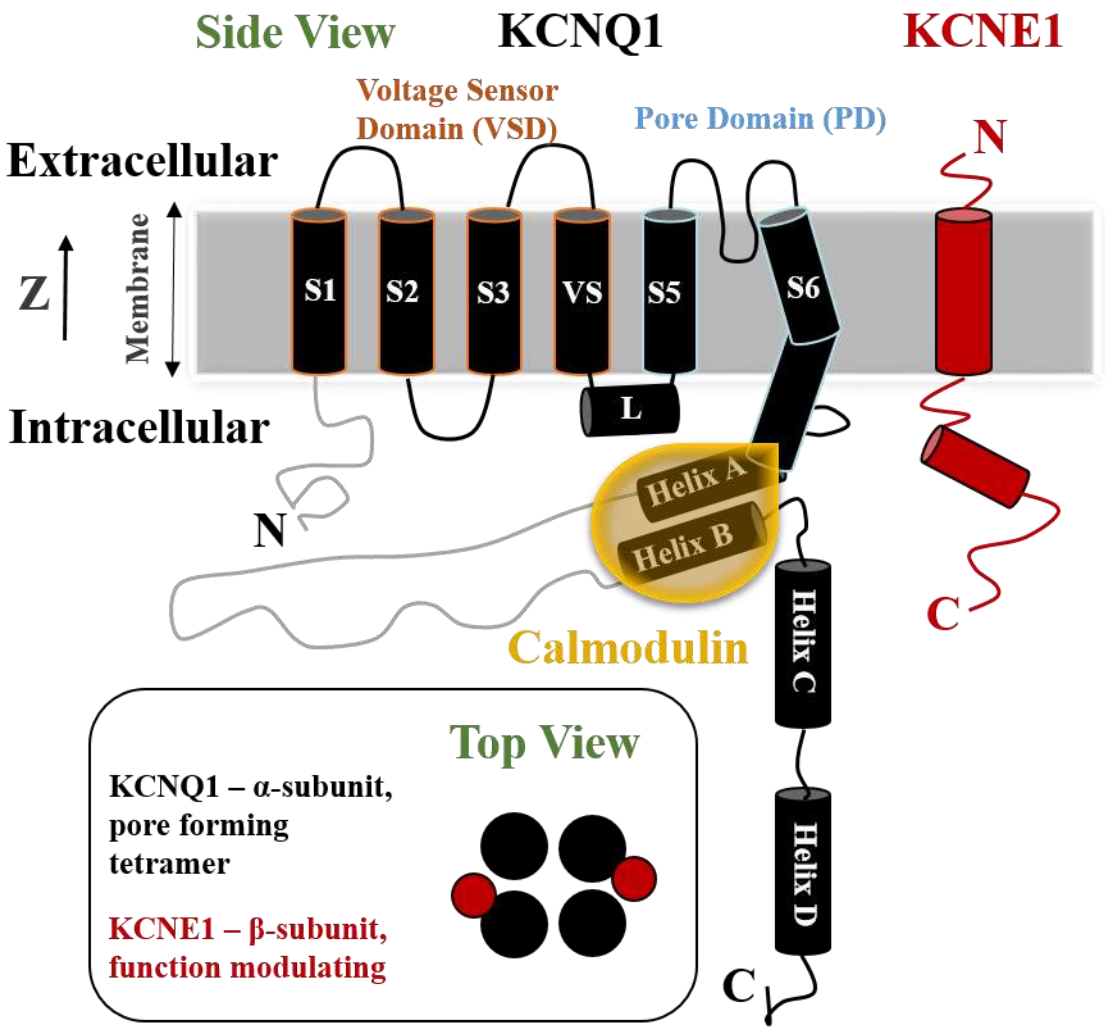

Figure S1. Schematic of KCNQ1 and KCNE1 segments. *The cylinders represent a-helices and the grey lines represent disordered protein segments that are not part of the structural model. The starting model of IKs is built based on this schema. N, C indicate the N- and C-terminus, respectively.*

** Note that in this figure and other figures of the supplement, symbols and corresponding structural elements are color-coded.*

Kv channels (voltage gated potassium ion-channels) assemble as a tetrameric structure. In the case of IKs, each of the four identical pore forming subunits (a subunits, KCNQ1) contain six transmembrane segments (S1-S6). Respectively, segments S1-S4 and S5-S6 constitute the VSD (Voltage Sensor Domain) and PD (Pore Domain). The P-loop in the PD features a selectivity filter that determines which cations pass through the pore. Accessory subunits (e.g. KCNE1, Calmodulin) modulate the function of the protein; these subunits bind and interact with different parts of the a subunits. The N-terminus of KCNQ1 (1-120 residues) and the 100 residue long linker between HelixA&B (HelixA and HelixB) are not modelled since experimental data suggest that they are disordered(1, 2). All other components of the IKs model are built using published structural data from experiments. In this paper, IKs refers to a Kv7.1 homogeneous pore forming tetramer with two KCNE1 subunits, positioned as shown in the top view

(A)

```
3LUT        ---CERVVINISGLRFETQLKTLAQFPETLLGDPKKRMRYFDPLRNEYFFDRNRPSFDAI
3LNM        HESSERVVINISGLRFETQLKTLAQFPETLLGDPKKRMRYFDPLRNEYFFDRNRPSFDAI
KCNQ1TM     ----------------------------------------HVQGRVYNFLERPTGWKCF
                                                     .   . * * ..  .:..:

3LUT        LYYYQSGGRLRRPVNVPLDIFSEEIRFYELGEEAMEMFREDEGYIKEEERPLPENEFQRQ
3LNM        LYYYQSGGRLRRPVNVPLDIFSEEIRFYELGEEAMEMFREDEGYIKEEERPLPENEFQRQ
KCNQ1TM     VYHFAVFLIVLVCLIFSVLSTIE-----------------------------------
            :*::     :   : . :    *

3LUT        VWLLFEYPESSGPARIIAIVSVMVILISIVSFCLETLPIFRDENEDMHGGGVTFHTYSQS
3LNM        VWLLFEYPESSGPARIIAIVSVMVILISIVSFCLETLPIFRDENEDMHGGGVTFHTYSQS
KCNQ1TM     ------------------------------------------------------------


3LUT        TIGYQQSTSFTDPFFIVETLCIIWFSFEFLVRFFACPSKAGFFTNIMNIIDIVAIIPYFI
3LNM        TIGYQQSTSFTDPFFIVETLCIIWWSFEFLVRFFACPSKAGFFTNIMNIIDIVAIIPYYV
KCNQ1TM     ----QYAALATGTLFWMEIVLVVFFGTEYVVRLWSAGCRSKYVGLWGRLRFARKPISIID
                * ::  *. :* :* : :::::. *::**:::. .:: :.    .:      *
                                        S4
3LUT        TLGTELAEKPEDAQQGQQAMSLAILRVIRLVRVFRIFKLSRHSKGLQILGQTLKASMREL
3LNM        TIFLTESNKSVLQFQ----NVRRVVQIFRIMRILRIFKLSRHSKGLQILGQTLKASMREL
KCNQ1TM     LIVVVASMVVLCVGSKGQVFATSAIRGIRFLQILRMLHVDRQGGTWRLLGSVVFIHRQEL
             :    :       .         :: :*::::*::::.*:.   ::**..:    :**

3LUT        GLLIFFLFIGVILFSSAVYFAEADERD----SQFPSIPDAFWWAVVSMTTVGYGDMVPTT
3LNM        GLLIFFLFIGVILFSSAVYFAEADERD----SQFPSIPDAFWWAVVSMTTVGYGDMVPTT
KCNQ1TM     ITTLYIGFLGLIFSSYFVYLAEKDAVNESGRVEFGSYADALWWGVVTVTTIGYGDKVPQT
               ::: *:*:*: *  **:** *  :     :* *  **:**.**::**:**** ** *
                                  S6
3LUT        IGGKIVGSLCAIAGVLTIALPVPVIVSNFNYFYHRE---TCERVVINISGLRFETQLKTL
3LNM        IGGKIVGSLCAIAGVLTIALPVPVIVSNFNYFYHRETHESSERVVINISGLRFETQLKTL
KCNQ1TM     WVGKTIASCFSVFAISFFALPAGILGSGFALKVQQKQRQ--------------------
              ** :.*  :: .:  :***. :: *.*    :::
```

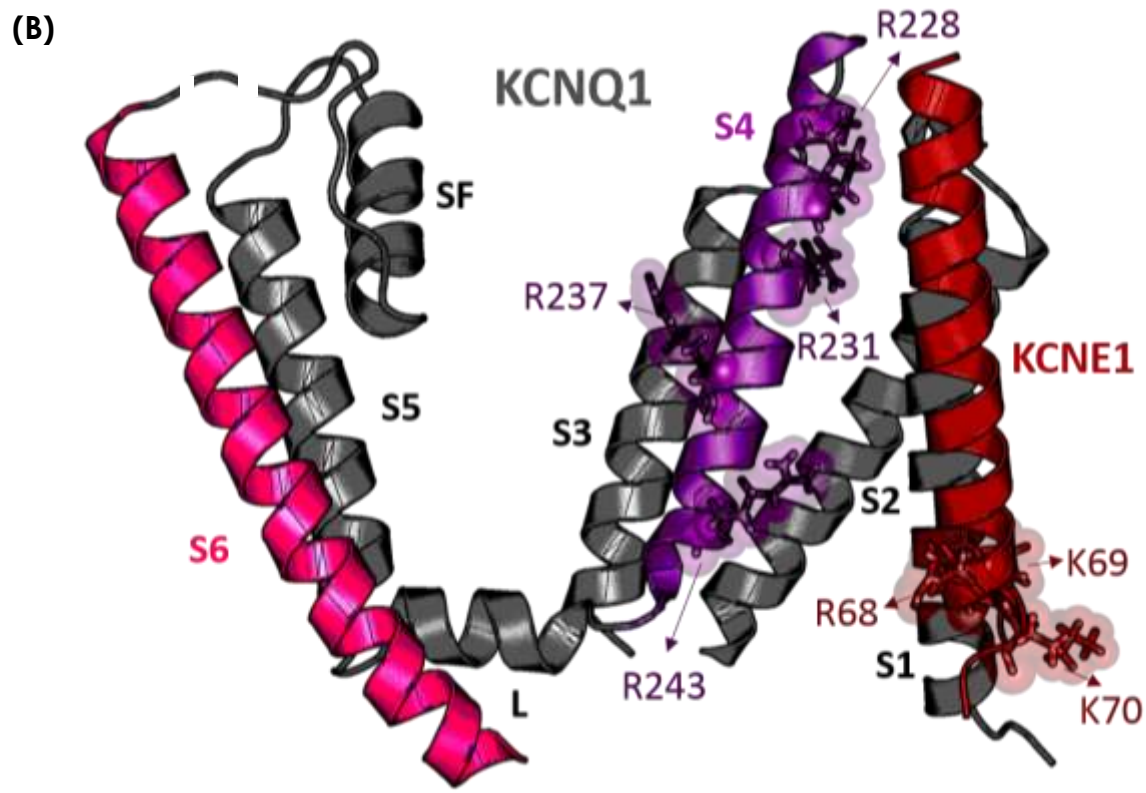

Figure S2. Homology model of KCNQ1 (homologous to Kv1.2/2.1) docked with NMR determined KCNE1 structure. *(A) Sequence alignment of KCNQ1 transmembrane domain with Kv1.2 (RSCB: 3LUT) and Kv1.2/2.1 (RSCB: 3LNM). S4 and S6 segments are highlighted, to correspond with panel B. (B) The resultant model of transmembrane KCNQ1-KCNE1 is shown, with important segments and charged residues that play a vital role in gating highlighted. Note that long linkers (S2-S3 and SF-S6) are not shown to provide better figure clarity. (L, S4-S5 linker; SF, selectivity filter; KCNQ1, a-subunit of IKs; KCNE1, β-subunit of IKs)*

Experimental structural data for KCNQ1 were not available at the inception of this project. Therefore, we applied homology modelling using Kv1.2

crystal structure data (3–5) to build the KCNQ1 transmembrane domain (previously published (6, 7)). Furthermore, Kv1.2/2.1 chimera crystal structure (8) was utilized to remedy any poor resolution segments of the Kv1.2 crystal structure and also fill in gaps of the aligned sequence (Figure S2A). This information along with attributes from previously published computational models (9) were incorporated in building the homology model of the KCNQ1 pore forming tetramer. The structure was further optimized using the Rosetta software (connecting loops and linkers) (10). Many conformations similar to the recently published experimental KCNQ1 structure (11) were sampled in the constructed IKs structure library (details in Section 2 and Figure S11).

The KCNE1 transmembrane helix is important for the functional modulation of the KCNQ1 tetramer. It is responsible for slowed activation and increased magnitude of current (12). Human KCNE1 structure has been determined using NMR (13–16). Many experimentally determined KCNQ1-KCNE1 interaction sites and structural models of KCNE1 docking have been published (3, 5). Rosetta FlexPepDock refinement protocol was used to further optimize the transmembrane interface between KCNQ1 and KCNE1 (17). Recently published KCNQ1/KCNE1 docking data show consistent results (18).

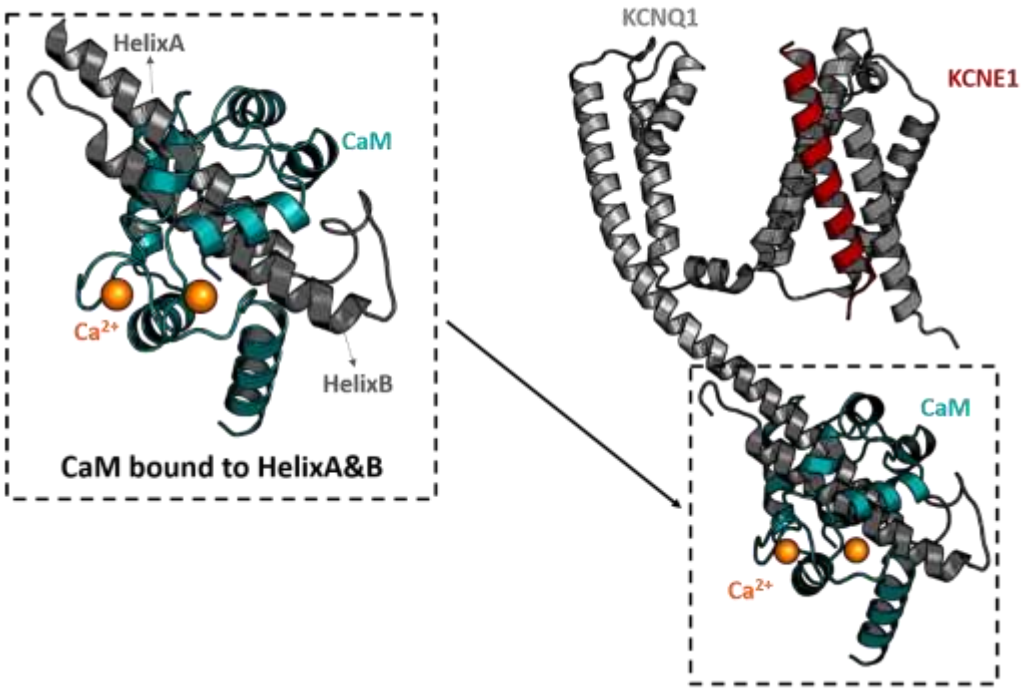

Figure S3. Incorporating CaM interactions with IKs. *The resultant structure after stitching together the transmembrane IKs complex and the crystal structure of HelixA&B is shown. The latter is bound to CaM with two Ca^{2+} ions (dashed box)* (19). *(CaM, Apo-calmodulin; Ca^{2+}, calcium ions; HelixA&B,* HelixA and HelixB*)*

Calmodulin is essential for channel assembly and gating; it mediates Ca^{2+} sensitive modulation of the IKs ion-channel (20–22). Mutations in calmodulin can disrupt current and the current-voltage relationship. Note that calmodulin in this section refers to Apo-calmodulin (a variant bound to 2 as opposed to 4 Ca^{2+} ions; CaM). This is the only calmodulin variant for which experimentally-determined structure was available, in the context of IKs ion-channels, when the protein structure was constructed.

Rosetta was used to minimize steric clashes of side-chains and extend S6 to HelixA using secondary-structure predictions of S6-HelixA amino acid sequence by the DSSP algorithm (23, 24). The latter is consistent with the ridged-lever arm attached to CaM near the proximal membrane region, as suggested by small-angle X-ray scattering data (19). Experimental observations also suggest that each HelixA and HelixB (HelixA&B) of individual KCNQ1 segment binds to CaM. Thus the complete IKs ion-channel model has a CaM bound to each KCNQ1 segment (4 KCNQ1: 4 CaM).

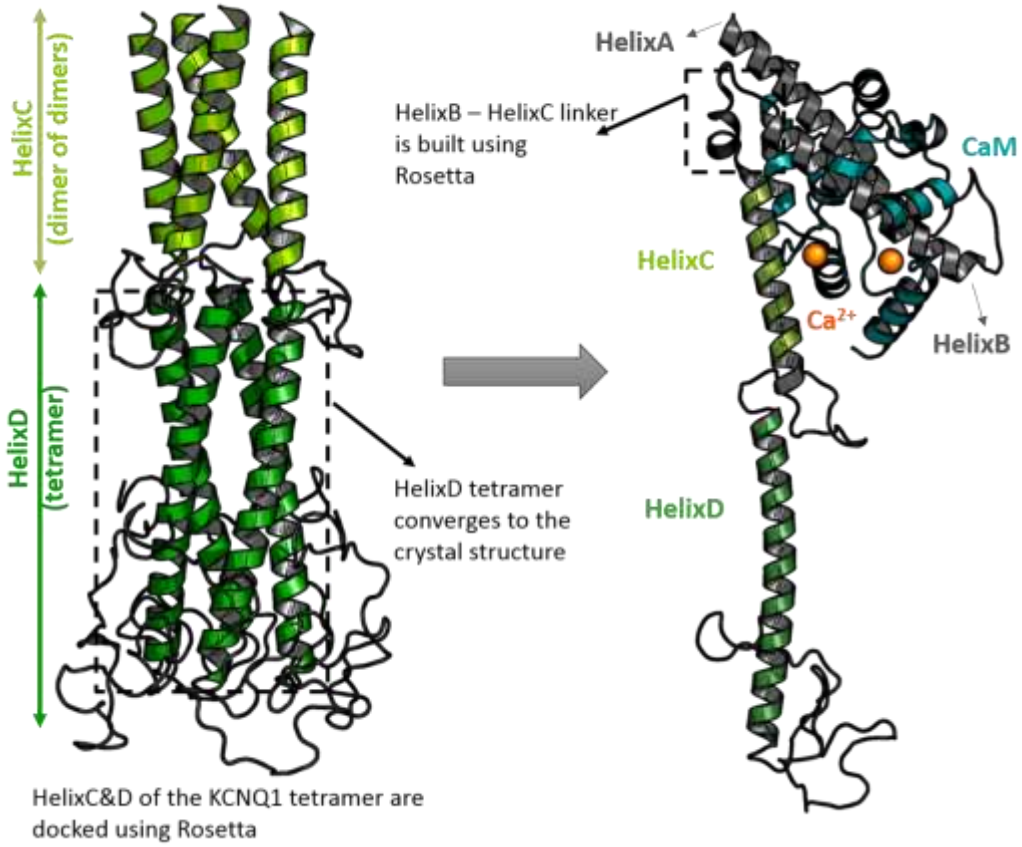

Figure S4. Rosetta docked model of HelixC&D. *HelixD tetramer of the docked model shows convergence to the published crystal structure. HelixC&D is connected to the HelixA&B model bound to CaM by a ten residue linker (built using Rosetta). (CaM, Apo-calmodulin; HelixA&B,* HelixA and HelixB; *HelixC&D, HelixC and HelixD)*

HelixC and HelixD (HelixC&D) secondary structure and interactions between these segments in the KCNQ1 tetramer have been investigated using experimental techniques such as CD spectroscopy and crystallography(1, 2, 25).

Using this information with the Rosetta module (26), HelixC&D segments of the KCNQ1 tetramer were docked and minimized for steric clashes. The resulting simulated HelixD tetramer shows convergence with its resolved crystal structure (2); RMSD comparison between the backbone atoms of the model and crystal structure is less than 0.13 Å. The linker between HelixC&D and HelixA&B of each segment is built using Rosetta to complete the C-terminus of the KCNQ1 tetramer.

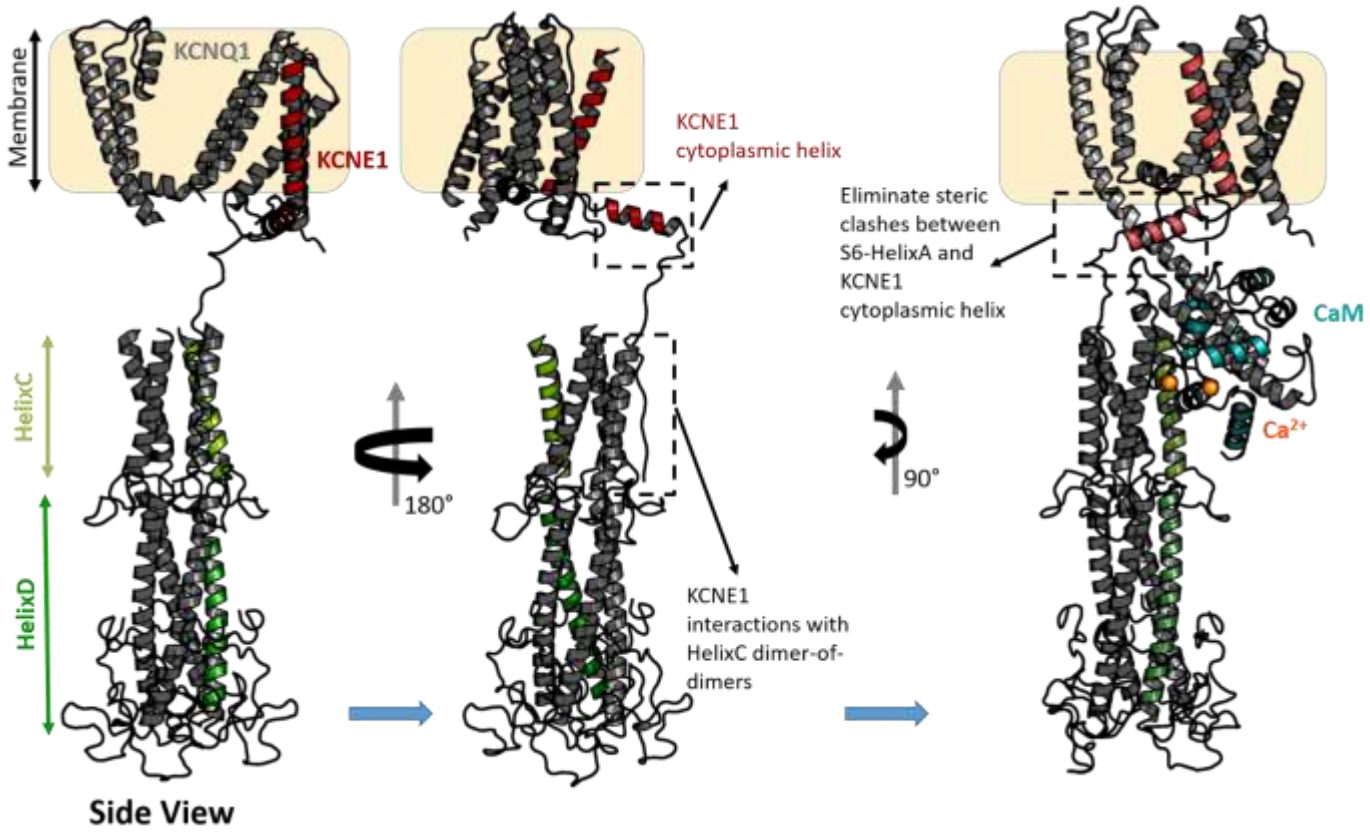

Figure S5. Side view of KCNQ1-KCNE1 interaction sites. *KCNE1 cytoplasmic interactions with HelixC dimer-of-dimers is resolved using Rosetta. The position of the cytoplasmic KCNE1 helix is adjusted to remove steric clashes and the linkers between KCNE1 C-terminus tail, KCNE1 cytoplasmic helix and KCNE1 transmembrane helix are built using Rosetta. Dashed-boxes and arrows represent interaction interfaces between KCNQ1 and KNCE1 in the cytoplasmic region.*

Rate dependent facilitation of IKs depends on the KCNE1 C-terminal interactions with KCNQ1 C-terminus (27). Mutations in the C-terminus region of

KCNE1 can produce defective rate dependence and thus cause arrhythmias (27). KCNE1 NMR data show a secondary helical segment, which is most likely in the cytoplasm (14, 15). Additionally, experiments have shown the C-terminal segment of KCNE1 interacts with the KCNQ1 HelixC coiled coil (1). This interaction is at the interface between two KCNQ1 segments and was resolved using the Rosetta module (17, 28). The linkers between the KCNE1 helical segments and C-terminal interaction site are also built using Rosetta. The KCNE1 cytoplasmic helix is adjusted to remove steric clashes (against S6-HelixA).

The IKs tetramer structure was minimized using MODELLER (29) (10,000 steps, interaction energy is minimized). Although the stoichiometry of KCNQ1:KCNE1 ratio is controversial, the expression levels in cardiac myocytes suggest at least a 4:2 ratio (30–34). Thus, two KCNE1 β-subunits were docked to the KCNQ1 tetramer (on opposite KCNQ1 subunit clefts).

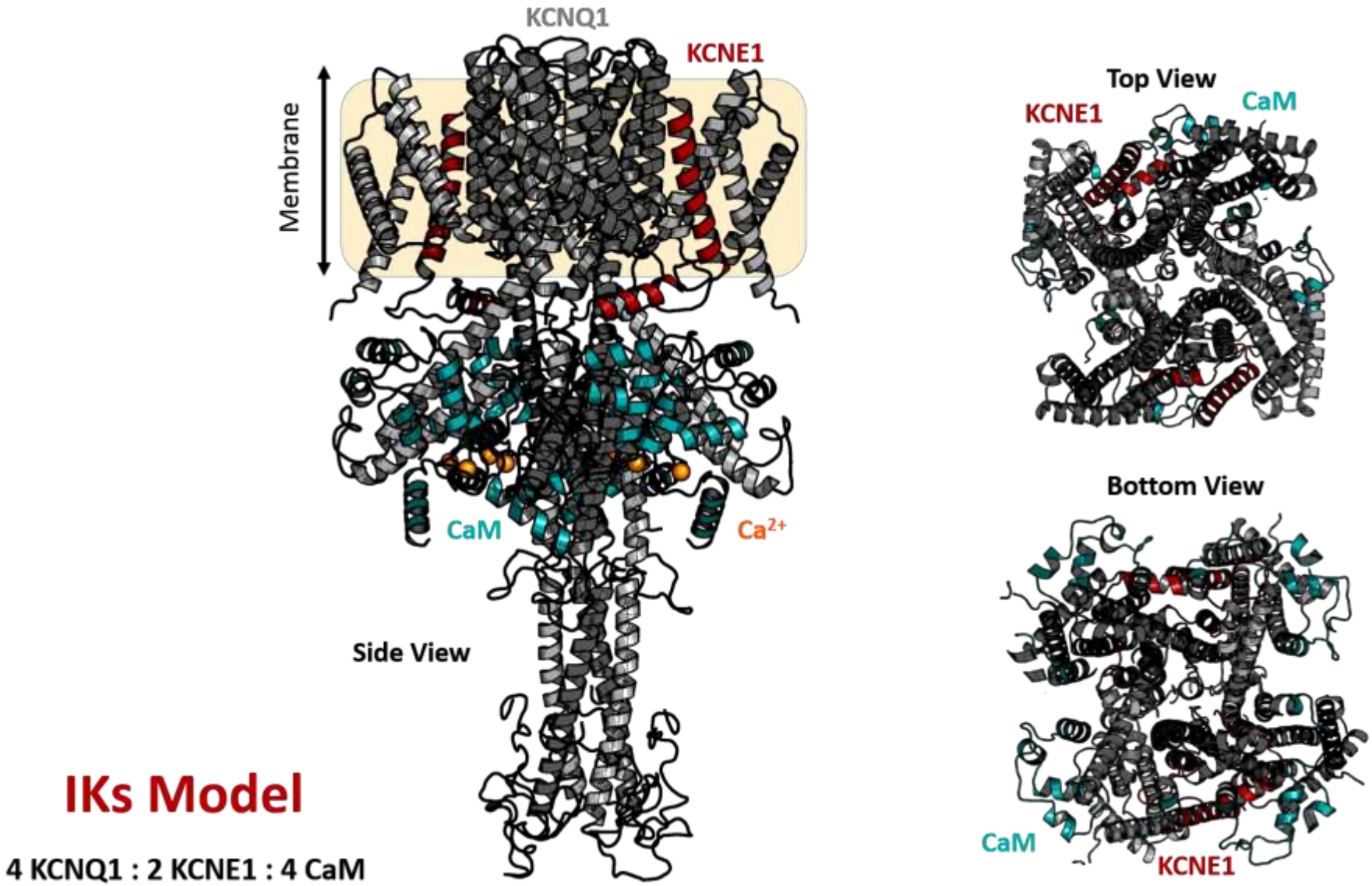

Figure S6. The complete structural model of *IKs. Side, Top and Bottom views*

Section 2

Methodology

Introduction

It is extremely challenging to computationally simulate the dynamics of large proteins such as ion-channels, in the milliseconds to seconds timescale that is necessary to study their physiological function, e.g. channel gating. The entire space of trajectories of protein conformational changes needs to be assessed in order to meaningfully understand the relationship between structure and physiological function. To achieve this, all possible conformations of the protein need to be constructed. This is an impossible task with a large protein such as the IKs ion-channel; the backbone of each amino acid has two rotational degrees of freedom (phi, psi) and its respective side chains include additional degrees of freedom. Even with a simplified structure, the IKs ion-channel has a total of 4836 degrees of freedom (2418 residues, without including sidechain degrees of freedom). When assessed with a coarse grain grid (phi and psi range [-180°, 180°], step 10°), this results in 1296^{4836} possible conformations during dynamics. Even if this computation were possible, the stratagem of using a coarse grid would reduce the structural resolution of the model and result in invalid physiological interpretations. Thus, a more economical approach is required to generate a library of conformations in a fine-grain grid and to estimate the respective structural energy for simulating dynamics. The outline for the approach developed and used in this study is detailed in Figure S7; the following sections provide the relevant details.

2.1: Sampling the IKs Gating Conformational Space and Energy Calculations

Generating a library of conformations for simulating ion-channel gating

From Experimental data, it is known that during gating (dynamics of the ion-channel in response to changes in membrane voltage (V_m)) the voltage sensor (VS, S4 transmembrane helix with positively charged residues) moves along with the S4-S5 linker (S4S5L), resulting in conformational changes of the pore (35–40). During membrane depolarization, VS moves upward (outward) towards the extracellular domain; it moves down (inward) during repolarization (Figure S8). This movement of VS can be characterized with 6 degrees of freedom (Figure S9).

In order to build a library of conformations that best represent the structural changes of the ion-channel during gating, VS of each segment in the KCNQ1 tetramer (Figure 1 in main text) was perturbed (translation and rotation with a resolution of 0.25Å and 0.1rad, respectively) in the dimensions shown in Figure S9. Experimental constraints (3, 41–48) were checked to ensure that the VS conformational change is physiologically possible. Next, the broken linkers between S3-S4 and S4-S5 were rebuilt (with Rosetta (49); the S4S5L is allowed to move within 0.25Å and 0.1rad) to accommodate this change in the VS conformation. Any steric clashes were eliminated and total energy of the protein was minimized (MODELLER (29); the backbone atoms of the VS were constrained to the new position). A representative schema of the aforementioned process is shown in Figure S10.

The electrostatic energy of the protein was calculated using Adaptive Poisson-Boltzmann Solver (APBS, APBSmem (50–54)) for different V_m. The membrane thickness was assumed to be 30Å (including 4Å ester headgroup of the lipid) and the dielectric of the protein, membrane, lipid headgroup and water used to calculate the energy was 2, 2, 80 and 80, respectively. Since the total energy of the protein has been minimized, only the electrostatic energy component of the total energy changes in response to changing V_m. The 3D coordinates of the protein structure and its electrostatic energy are tabulated at the end of each VS conformational change for different V_m.

To ensure that the conformational space of VS was searched effectively and efficiently, a rapidly-exploring tree algorithm is used (55–59). At each iteration, a new conformation is sampled at random and if this conformation meets the experimental constraints, a node is attached to the tree and the process continues. The probability that a node will be chosen for expansion depends on the volume of the unexplored region in the proximity of the node and consequently the tree will rapidly grow in unexplored regions of the conformational space. Assumptions used while building the library include: the backbone of secondary structures of the protein (helices and beta sheets) are considered to be rigid. Membrane and water/ions are considered implicit during energy calculations.

Previous papers have reported conformational libraries of the KCNQ1 tetramer (6, 7, 60). However, this library is unique in that it ***does not*** assume

(1) Movement of the 4 VS in the tetramer is symmetric,

(2) S3 and S4 move together ("paddle motion"(61, 62))

(3) Immobility of "static" segments (other than S3-S4, S4S5L and S6; both backbone and side chain)

(4) Mechanical coupling between VS and S6 via S4S5L - i.e. higher Z position of S4 results in wider pore.

(5) Allosteric gating mechanism - i.e. all 4 VS segments have to be in a relatively high Z position in order for the pore to open ("cooperativity").

Additionally, this library includes the complete structure of IKs, modelled with the available experimental data (refer to Supplement Section 1). The structure was not constrained with any non-physiological parameters e.g. application of extremely high V_m. Furthermore, the degrees of freedom of the entire structure were not limited or reduced and were allowed to change in response to the perturbed VS conformation.

Note that the 'pore diameter' is measured as the minimum distance between side-chain residues at the activation gate of the pore (63). Although the IKs pore does not have the 'PVP' (proline-valine-proline) kink in the S6 segment like Kv1.2, it does have a 'PAG' (proline-alanine-glycine) motif that results in a gradual bend. Nevertheless, the activation gate is assumed to be in the same region of S6 (below the cavity, in the interface between the membrane and cytoplasmic region).

The library of conformations were built before the recent KCNQ1 cryo-electron microscope (cryo-EM) experimental data (RSCB: 5VMS, (11)) was made available.

Therefore, this new structural data served to validate the extensive *de novo* sampling by our structure library of the IKs conformational space. The library samples many conformations similar to the cryo-EM structure (chain A, transmembrane segment) and one such conformation with the smallest small root-mean-squared error (RMSE; comparing backbone atoms) to 5VMS is shown in Figure S11. The largest backbone fluctuations occur at linker positions and the S1, S2, S5, P-loop and SF show very small fluctuations. Thus, the library is able to sample all possible conformations of the IKs gating space, including a possible (experimentally determined) KCNQ1 conformation.

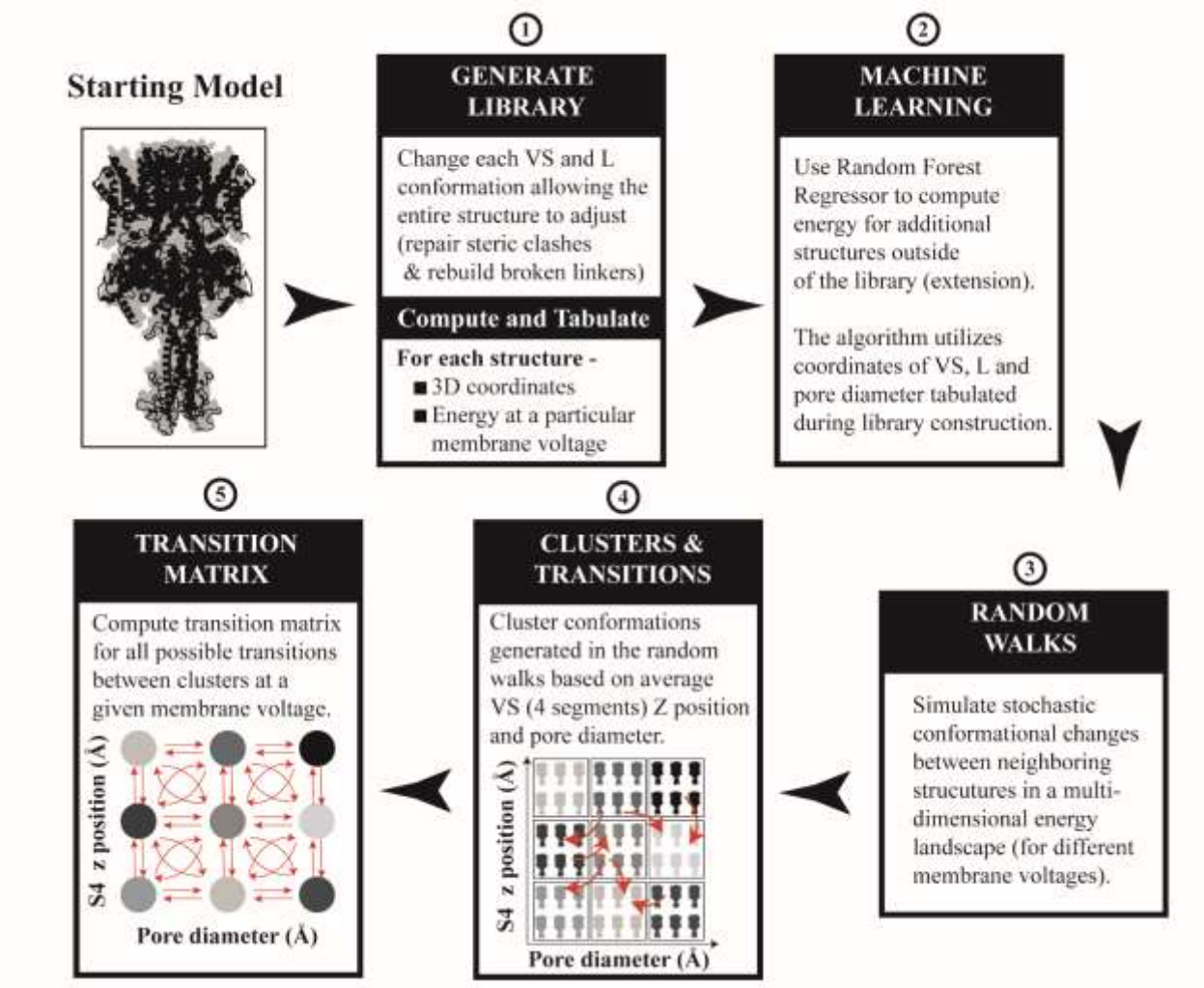

Figure S7. A flow chart for simulating protein dynamics.

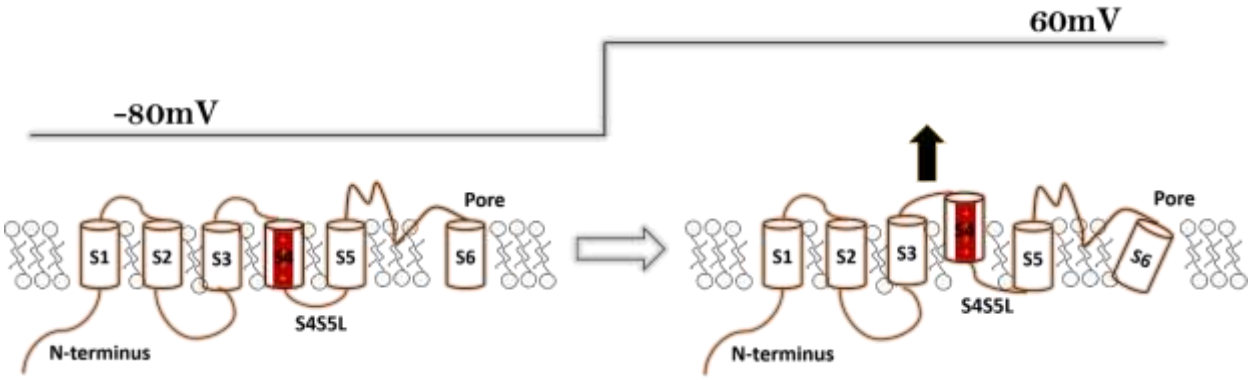

Figure S8. A cartoon representing the upward/outward motion of VS (S4) during depolarization. *The VS moves towards the extracellular side of the membrane in the Z-direction (perpendicular to the membrane) with some rotation. The S4S5L and S6 also move to accommodate this change. (VS, Voltage Sensor; S4S5L, S4-S5 linker)*

Range of Movement

X	Y	Z
[-10,10] Å	[-10,10] Å	[-20,20] Å

Pitch	Roll	Twist
[-π,π) rad	[-π,π) rad	[-π,π) rad

Resolution

X,Y,Z	Rotation
0.25 Å	0.1 rad

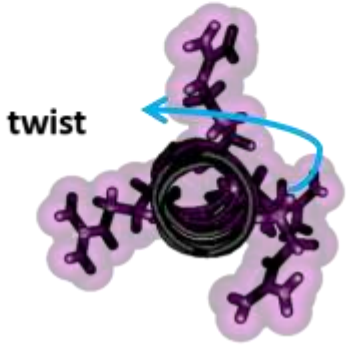

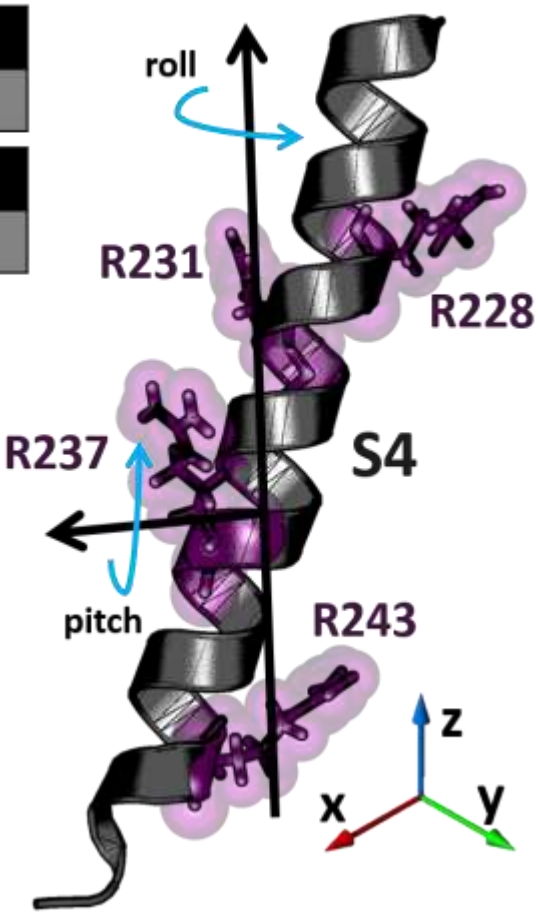

Figure S9. Degrees of freedom of Voltage Sensor (VS). *The VS is translated and rotated in X, Y, Z and pitch, roll and twist dimensions. The translation and rotation resolution is 0.25Å and 0.1rad, respectively. Positively charged arginine residues are identified (purple). (VS, Voltage Sensor (S4))*

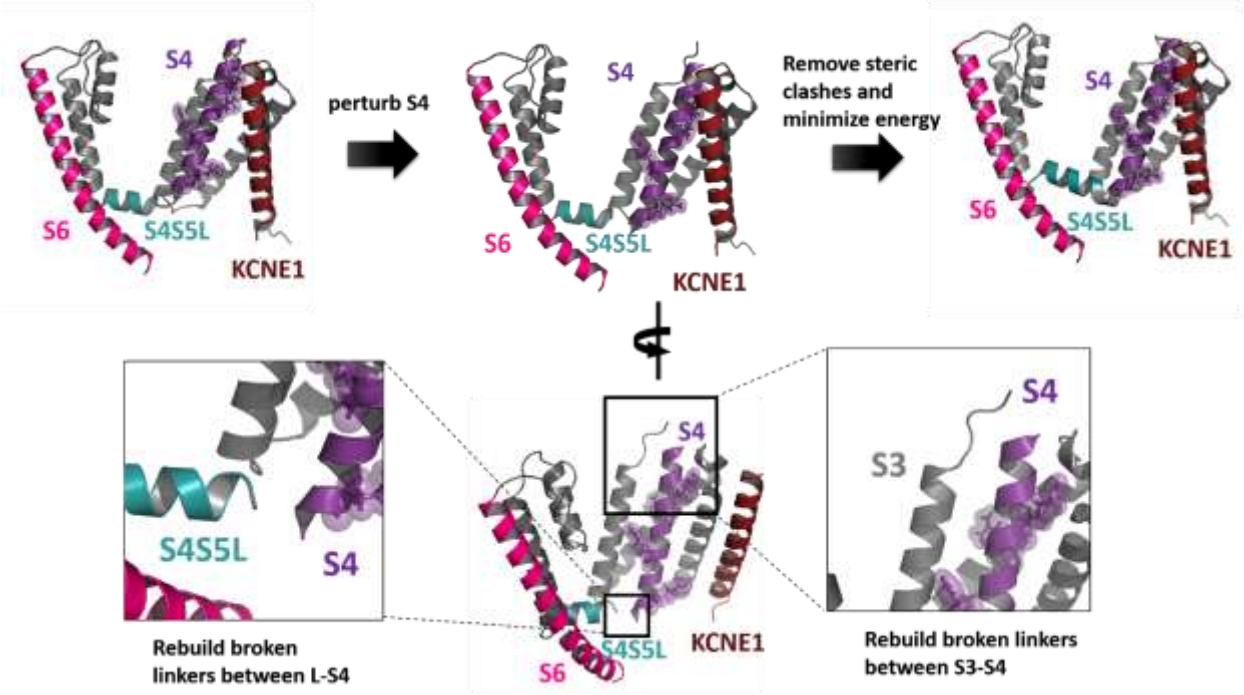

Figure S10. Perturbing VS (S4) and rebuilding structure. *The figure shows a schema going from the starting structure to the final minimized conformation. Steps include perturbing VS, rebuilding broken linkers, removing steric clashes and minimizing the total energy of the protein. Note that the VS arginine residues (R228, R231, R237, R243) are marked as sticks to show rotation (refer to Figure S8). (VS, Voltage Sensor (S4); S4S5L, S4-S5 linker; KCNQ1, α-subunit of IKs; KCNE1, β-subunit of IKs)*

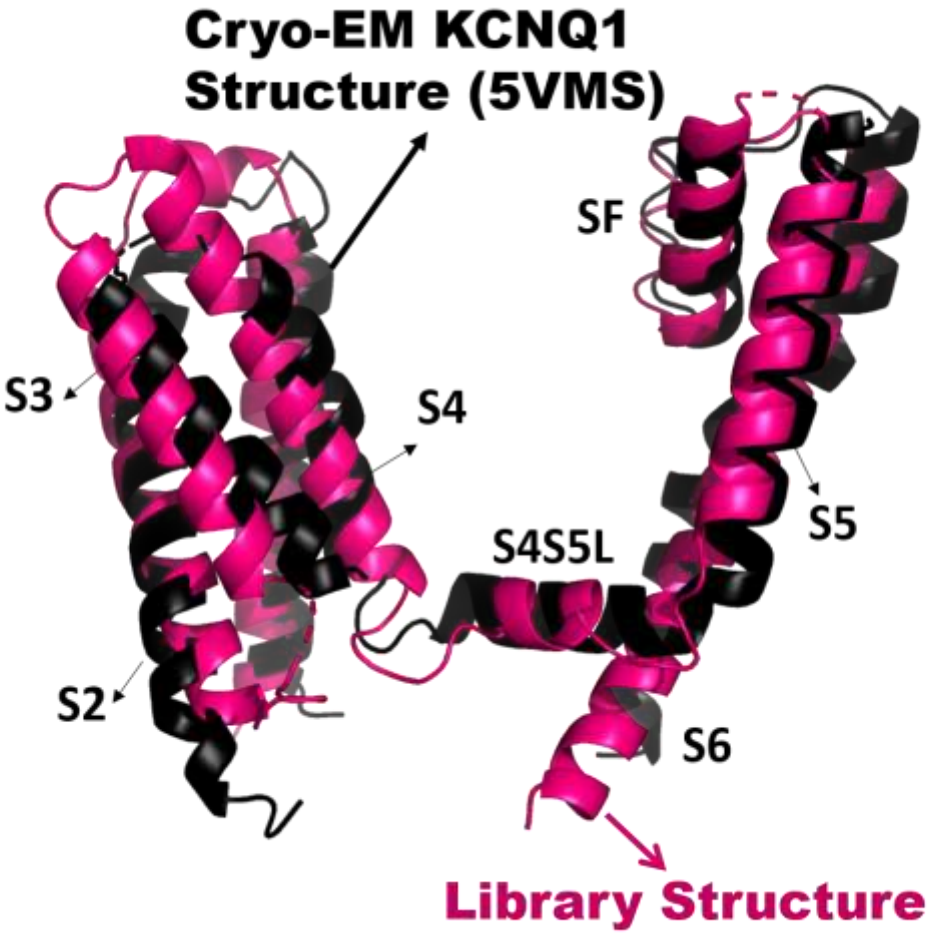

Figure S11. Comparison of 5VMS cryo-electron microscope KCNQ1 (chain A) structure to a library conformation. *The library conformation (118T-358K; pink) with the smallest backbone root-mean-squared error of 0.92Å aligned with 5VMS (108T-348K; black). The 5VMS transmembrane segments are labelled S1-S6. Note that long flexible linkers (S2-S3 and Ploop-S6) are omitted from this calculation.*

Energy calculations

The non-electrostatic energy components of the total protein energy were calculated with NAMD Energy plugin (with VMD (64, 65)) and the electrostatic energy was calculated using ABPSmem using CHARMM parameters (50, 52, 66) (at different V_m). APBS (67) is a well-established and tested computation method to calculate electrostatic energy of proteins as precisely as possible using implicit dielectrics. Multiple levels of field focusing were considered in these calculations by iteratively computing protein electrostatics with a coarse grid followed by similar calculations on a finer grid with boundary conditions determined from the former (coarse) run. A set of conformations are chosen randomly from the library and energy statistics (mean and standard deviation) were calculated. More conformations from the library were added iteratively to the latter set until the difference of consecutive calculation was less than 1%. Energy components of the protein (of randomly chosen 571,775 unique conformations from the library) show that the electrostatic energy contributes most to the total protein energy (Figure S12). The energy difference of the aforementioned conformation set at different V_m (-80mV and 60mV) show that the electrostatic energy changes are large (Figure S13). Therefore, the electrostatic energy contributes most to changes in protein energy that depend on V_m. In contrast, energy components other than electrostatic energy do not change with V_m and contributed much less to the total protein energy and thus are not utilized to calculate IKs gating dynamics.

Please note that henceforth all references to energy refer to the electrostatic energy calculated using APBS, unless explicitly stated otherwise. Additionally, total

protein energy in this subsection was computed as the sum of conformational and non-bonded energies (i.e. bond, angle, dihedral, improper, van der Waal, and APBS electrostatic energies).

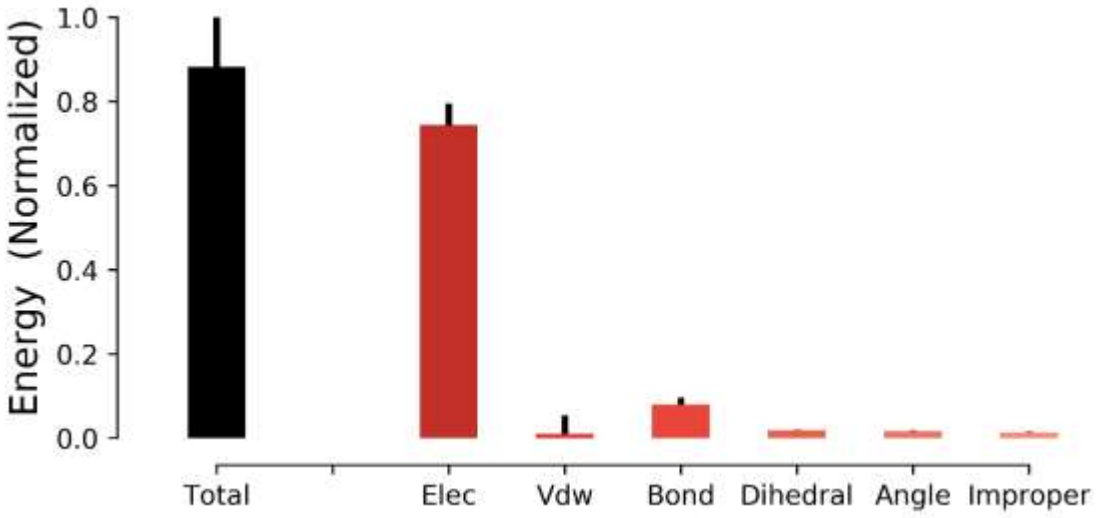

Figure S12. Energy components (normalized to total energy). *Protein energy calculated at 0mV shows that the electrostatic energy contributes ~85.5% of total energy of the protein. The bar plot shows the mean and standard deviation of 571,775 randomly chosen library conformations. NAMD Energy plugin (with VMD (64, 65)) was used to calculate non-electrostatic energy components of IKs conformational energy. APBSmem was used to calculate electrostatic energy. (Elec, electrostatic; Vdw, van der Waals)*

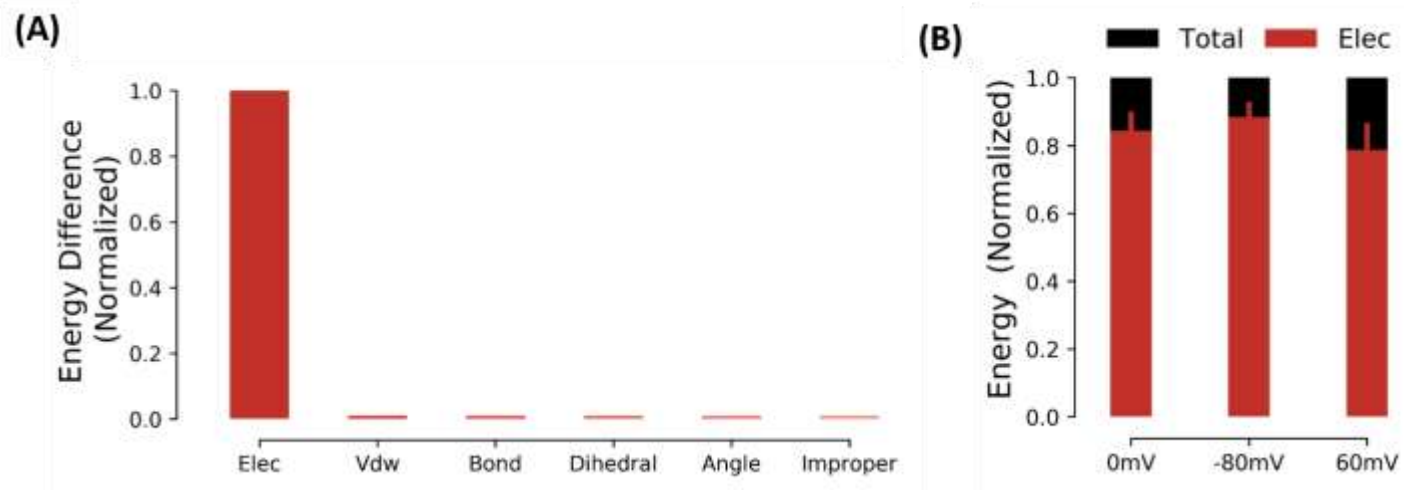

Figure S13. Electrostatic Energy contributes over 75% to total protein energy even at different membrane voltages. *(A) Mean energy difference of protein structures at V_m -80mV and 60mV. The data are normalized to the electrostatic energy difference and relative ratios show that electrostatic energy contributes most to IKs conformational energy changes that depend on V_m. (B) The relative ratios of electrostatic energy to total energy at V_m of 0mV, -80mV and 60mV. The electrostatic energy contribution is shown to be dominant over a range of physiological V_m. Note that the library structures used in this analysis were the same as in Figure S12. (V_m, membrane voltage; Elec, electrostatic; Vdw, van der Waals)*

2.2: Application of Machine Learning for Constructing the Protein Energy Landscape

Although the generated library of conformations is extensive and examines many degrees of freedom, it does not contain all possible conformations required to construct the ion-channel energy landscape during gating. A novel aspect of this study is the prediction of structural energy using Machine Learning (ML) algorithm. Using conformational features obtained from the protein 3D coordinates (tabulated from the library; section 1), The ML algorithm can compute energy of structures outside the library and thus enable the required extensive exploration of the energy landscape.

Choosing features to train the ML Algorithm

The structural energy to be predicted depends on the placement of charged atoms in the protein conformations. The majority of atoms position change occurs at the VS and S4S5L segments of the tetramer (refer to Section 1). Position changes of atoms in other segments are smaller (0.1-0.6Å) and contribute little to the change in energy (except S6, HelixA and Calmodulin; but most of these segments are in the cytoplasm and thus shielded from the transmembrane segments). Therefore, using the 6 dimensions of VS and S4S5L (48 dimensions in the tetramer) as features for training the ML algorithm to predict energy was expected to be an effective strategy. The same set of features was also suitable for training the ML algorithm to predict the

diameter of the pore during a random walk, as changes in these features result in altered pore conformations.

ML: The random forest algorithm

The random forest algorithm (68) is an estimator that fits varying branches of decision trees with varying sub-samples of the training data. An extended tree regression algorithm with 2500 trees (69, 70) was used to predict the structural energy of a conformation given its VS and S4S5L features. To train and implement the ML, the library was divided into training and testing sets with no overlaps. The ML is "trained" recursively with the training set and uses averaging to prevent over-fitting. When the regression algorithm works, it will predict the energy of the test set of structures with minimum error (Figure S14).

The features extracted from the structural library were pre-processed with Principal Component Analysis (PCA; (71–73) and the energy values were scaled between [-1, 1] to increase the accuracy of the ML. PCA showed that all 48 features of the protein were important to completely represent the conformation. Also, 1.5 to 3 million structures were required to train the ML to predict the energy with acceptable accuracy (Figure S14.A). Using this technique, the libraries of IKs structures were trained with ML to predict their structural energy (Figure S14.B).

The MSE (Mean Squared Error) is calculated between the predicted and the actual energy values (recorded in the library) for corresponding testing structures not used to train the ML. The MSE decreases with increased size of the training set. The

convergence ensures that the ML can predict the energy of structures outside the library with acceptable accuracy. A similar technique was used predict the pore diameter of a structure; it also showed similar convergence with 3 million structures in the library.

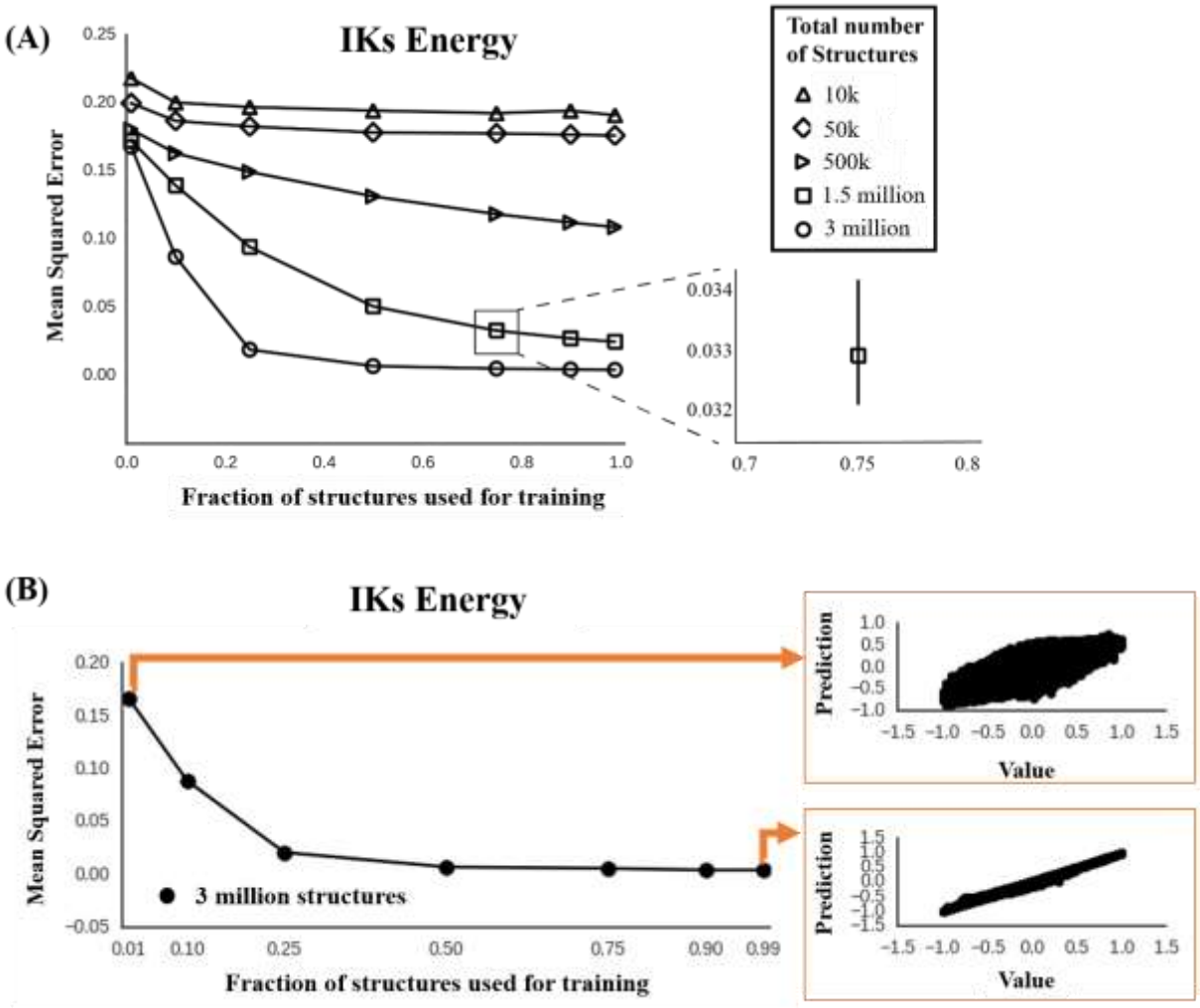

Figure S14. Training the Machine Learning algorithm (ML). *(**A**)The fraction of total structures (from the library) plotted against the Mean Squared Error (MSE) shows convergence with increased size of the training set. Excellent convergence is obtained with 50% and even 25% of the structures in the training set from a total of 3 million structures in the library. The inset shows zoomed in MSE with error bars (library of 1.5 million structures, 10 runs) (**B**, left) Similar plot to Panel A. (B, right) The ML predicted energy values plotted against the actual energy values from the library using a training*

set of 1% (top) and 99% (bottom) structures (randomly chosen from library). (MSE, Mean Squared Error; ML, Machine Learning)

2.3: Random walks, conformational clusters and building a structure-based Markov Model

Since the energy landscape of the protein at a particular V_m is of high dimension, it is impossible to search and visualize energy barriers and minima by observation. Random walks (stochastic structural changes based on chosen features) with different starting points on the energy landscape using the Metropolis-Hastings criterion (74, 75) provides a quantitative probability of transitions between different regions of the energy landscape. The latter approach also negates the need to calculate the partition function which would otherwise require the calculation of all possible transitions on the energy landscape. Thus, thirty random walks were simulated for 500,000 steps at different V_m and the resulting trajectories were recorded for further analysis

Clustering the structures that were visited in the random walks in dimensions of interest and physiological relevance (average VS Z position and pore diameter) further reduces the dimensions for visualization and analysis. By counting the transitions between different clusters from the random walks transition rates can be estimated (76). The resulting transition matrix was used to calculate structural changes of the protein given a particular V_m. Note that the structural clusters constitute Markov states in a Markov Model with transition rates between the states represented by the transition matrix.

Also note that the analysis was performed with structures clustered on an evenly spaced 45 by 9 grid in the pore diameter and average VS Z position dimensions (a total of 405 clusters). Note that additional features of protein structure could be included in the ML training in order to study other structure-function mechanisms.

2.4: Gating Mechanism Calculations

Gating charge calculation

The displaced gating charge was calculated using Adaptive Poisson-Boltzmann Solver (50); likely conformations of the IKs at holding potential and various steady-state depolarizing V_m were utilized in these computations. A likely IKs conformation in this computation was chosen based on its probability of being visited at a particular V_m.

Sequential Gating Analysis

The structures were alternatively clustered based on the movement of the four individual S4 segments in the Z-direction and movement of the pore. This results in a five-dimensional Markov chain (four S4 Z and one PD). Note that the SC of the control structures were re-estimated for the different clustering in this section and were utilized with the various suppressed S4 segment models. The individual S4 Z translation was segmented into 4 equally spaced clusters (between -15Å and 15Å) and the PD was discretized to 6 levels (level 0 was considered to be closed pore and levels 1-5 open pores with varying SC), resulting in 1536 structure clusters. Each cluster had a unique combination of the 5 dimensions (four S4 Z and one PD). To simulate function, movements of individual S4 in the Z-direction were incrementally suppressed (not

allowed to move during random walk simulations) and transition rates were used to construct the corresponding Markov model.

Residue pair interaction calculations

Residue interaction calculations were used to ascertain the important residue interactions that contribute to dynamics during IKs gating. Positively and negatively charged residues contribute more to the total electrostatic energy of the protein than neutral residues. Thus, important charged residues interactions that contribute to iCh gating were identified using an *in silico* residue charge neutralization method. For example, APBS was used to obtain the contribution of a residue of interest, say Residue A, to the protein electrostatic energy. Additionally, the residue's interaction strength to other residues was calculated, for example, to Residue B. The interaction between Residue A&B was obtained by neutralizing Residue B (setting the charge to zero) and recalculating Residue A's contribution to the protein energy. The difference was recorded as the 'interaction energy' between Residue A and Residue B at a certain S4 Z position and membrane voltage (60mV). Residue A's contribution to protein stabilization (a measure of interaction favorability) is also an important measure for assessing the importance of its interactions with other residues. Therefore, simultaneous assessment of the strength of the interactions and contribution to protein stabilization is provided for residues in the VS domain positioned far away and close to the KCNE1 transmembrane segment.

Section 3

Results

Introduction

Using IKs single-channel experiments (77) and pore electrostatic profile (main text, Figure 2B), a subconductance (SC) were assigned to each structure cluster modelled from a library of possible gating conformations. These calculated SC are used to simulate functional properties of the IKs model. In this section, additional single-channel statistics are shown for discreet SC levels. Supplementary analysis and simulations were performed to examine the mechanism of S4 Z movement and gating charge saturation at positive V_m. Residue-residue interactions were also analyzed to understand the atomistic interactions that govern IKs gating. The following sections corroborate the model's ability to simulate both the functional and structural changes of the IKs ion-channel during gating.

3.1: Simulated Single Ion-channel Functional Analysis

The main text (Figure 3) shows simulated single-channel characteristics and its comparison to experiment (77). Other single-channel functional statistics, including latency to first opening, probability of 1st opening, total dwell time and mean open time, calculated from the simulated traces at different V_m are provided in this sub-section. The statistics were tabulated based on discrete SC levels (main text, Figure 2B). Structures with the highest conductance have high Avg.S4Z position (average Z position; over 4 VS in the tetramer) and large pore diameter (PD) as compared to other structures. The total dwell time averaged over 1000 traces showed high SC levels were accessed for longer periods with

increased V_m. Mean open times show that at 80mV, the ion-channel resides for long periods of time at the highest SC level, similar to 60mV, resulting in larger current. Using a threshold of 0.5pA, the latency to first opening was calculated for different membrane potentials. At 60mV, the latency value of 1.65 ± 0.08 seconds is very similar to the experimentally measured value of 1.67± 0.008 seconds. The latency to 1st opening decreased with increased V_m, as expected. The probability of 1st opening at different SC levels increased with time, also as expected. With increased V_m, the ion-channel is more likely to open earlier, as shown in Figure S16.

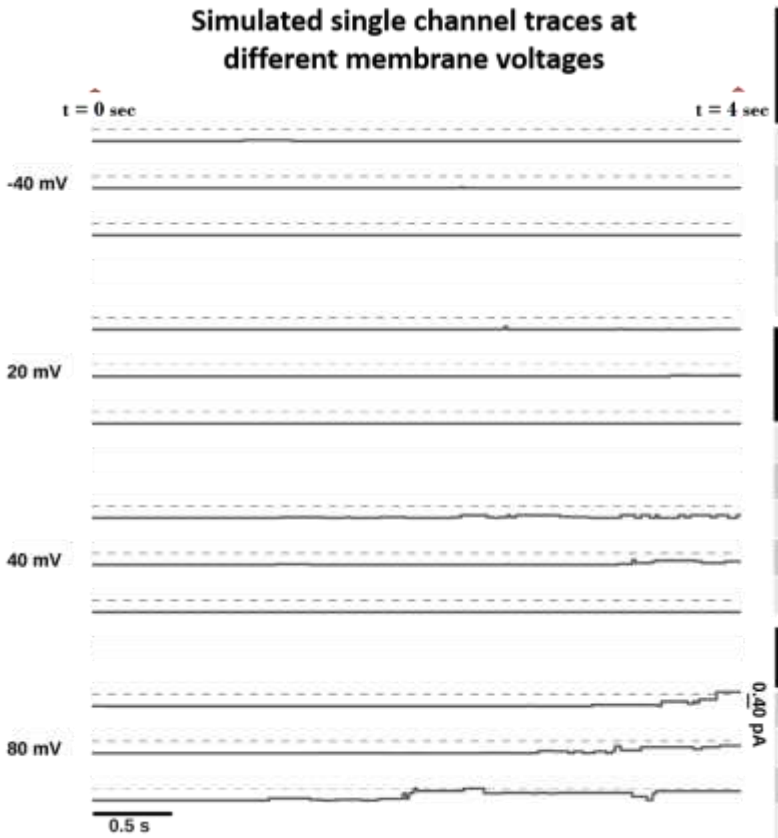

Membrane Voltage	Total Dwell Times (average over 1000 single channel traces; seconds)				
	I	II	III	IV	V
-40 mV	0.183	0.398	0.700	0.139	0.024
20 mV	0.176	0.453	0.715	0.138	0.019
40 mV	0.183	0.415	0.730	0.194	0.095
60 mV	0.206	0.436	0.712	0.344	0.081
80 mV	0.197	0.474	0.738	0.346	0.089

Membrane Voltage	Mean Open Times (1000 single channel traces; seconds)					
	I	II	III	IV	V	Total
-40 mV	0.089	0.097	0.093	0.027	0.080	0.386
20 mV	0.074	0.095	0.093	0.099	0.087	0.448
40 mV	0.079	0.086	0.094	0.085	0.090	0.434
60 mV	0.087	0.076	0.087	0.098	0.116	0.464
80 mV	0.075	0.089	0.081	0.091	0.176	0.512

Membrane Voltage	Latency to 1st Opening (threshold 0.5pA; seconds)
-40 mV	-
20 mV	-
40 mV	2.67 ± 0.01
60 mV	1.65 ± 0.08
80 mV	1.77 ± 0.01

I (0.93-1.4pS) II (1.4-2.07pS) III (2.07-3.14pS) IV (3.14-4.7pS) V (4.7-5.4pS) Total = I+II+III +IV+V

Figure S15. Single-channel Statistics. *(**Left**) Single-channel traces simulated at different depolarizing* V_m *from a holding potential of -80mV for 4 seconds. (**Right**) Table of the total dwell time, mean open time, and latency to 1st opening, for 1000 simulated single-channel traces (examples shown in the left panel). The temporal resolution of the calculations is 0.018 msec. The discrete subconductances used to classify the calculations are*

obtained from main text, Figure 2B. The corresponding SC range of each discrete level is shown in the bottom-right of the figure. (V_m, membrane voltage; SC, subconductance)

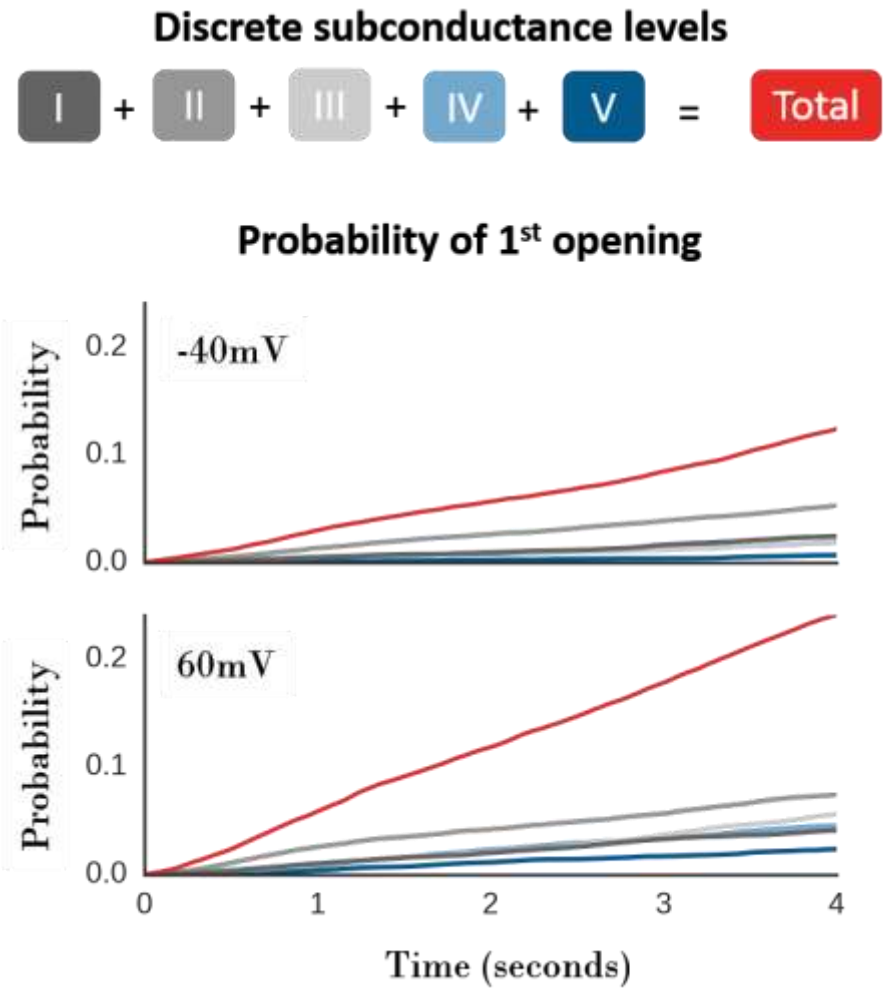

Figure S16. Probability of 1st opening. *The Probability of 1st opening is shown for each discrete SC level for a step depolarization to -40mV (**top**) and 60mV (**bottom**) from a holding potential of -80mV. The probability of 1st opening increases faster at all SC levels for a depolarizing voltage of 60mV as compared to -40mV. The calculations were performed based on discrete SC levels identified in main text, Figure 2B. The probability traces are color coded by SC level (shown on top; total conductance shown in red). (SC, subconductance)*

3.2: Residue Interactions that Govern IKs Gating (Voltage Sensor Movements)

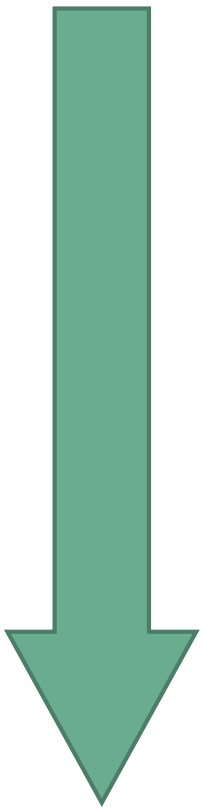

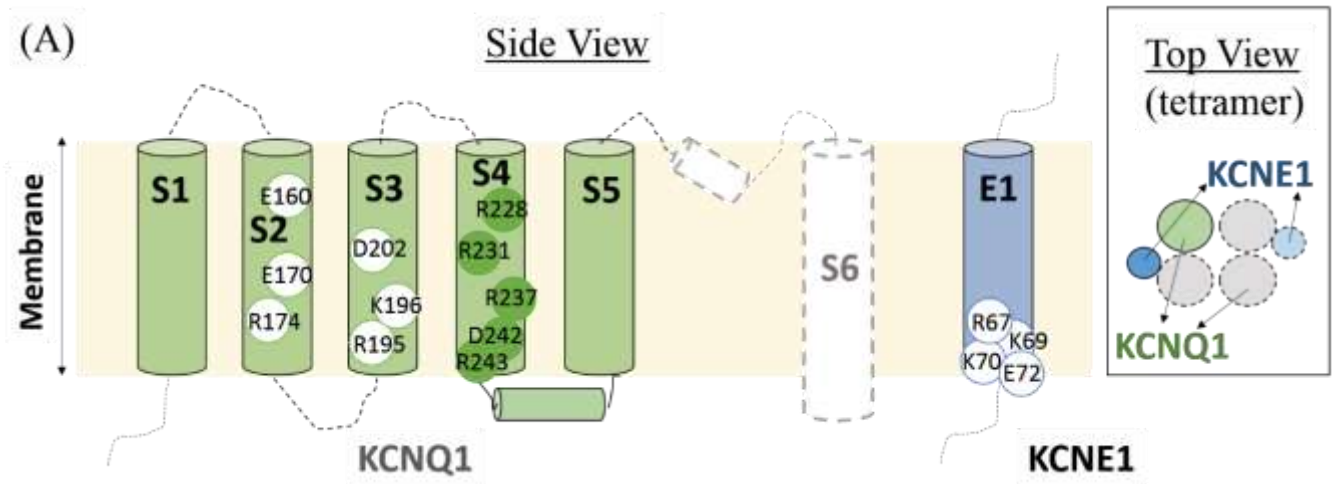
(A)
Side View
Membrane
S1
S2
E160
E170
R174
S3
D202
K196
R195
S4
R228
R231
R237
D242
R243
S5
S6
E1
R67
K69
K70
E72
KCNQ1
KCNE1
Top View
(tetramer)
KCNE1
KCNQ1

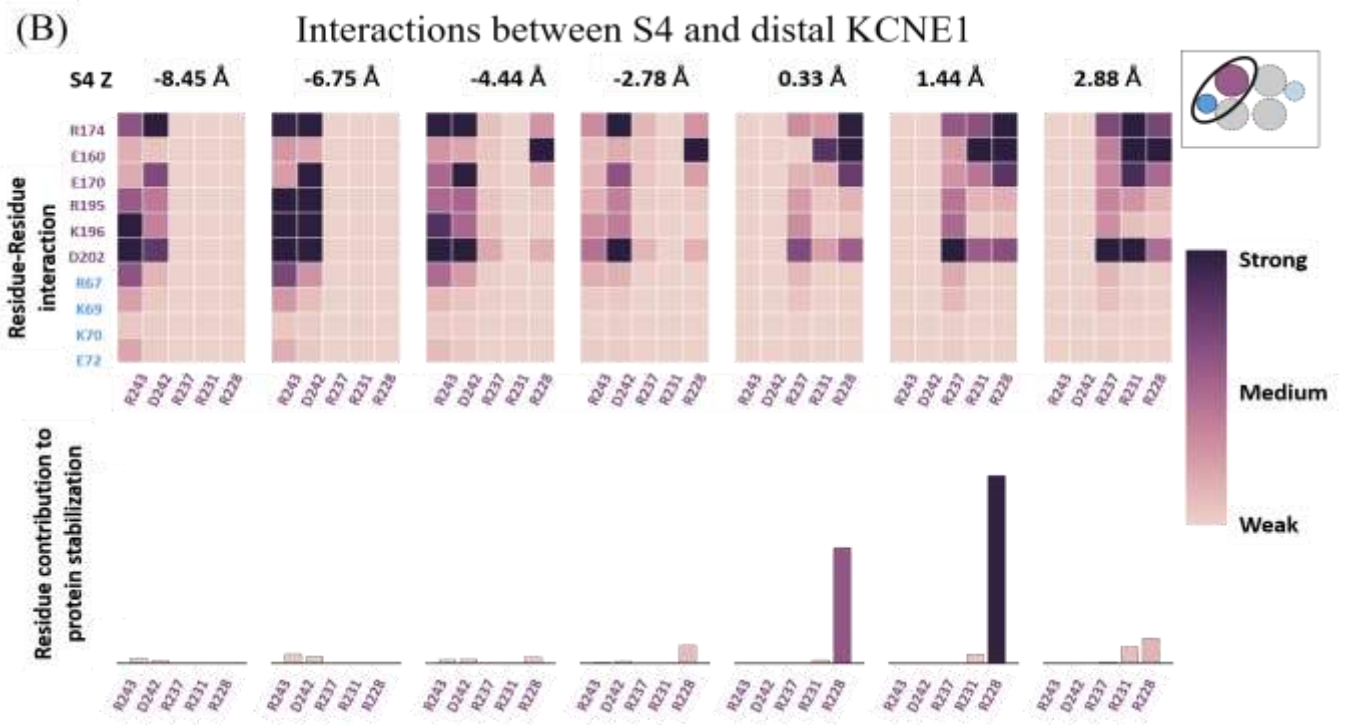
(B)
Interactions between S4 and distal KCNE1
S4 Z
-8.45 Å
-6.75 Å
-4.44 Å
-2.78 Å
0.33 Å
1.44 Å
2.88 Å
Residue-Residue interaction
R174
E160
E170
R195
K196
D202
R67
K69
K70
E72
R243
D242
R237
R231
R228
Strong
Medium
Weak
Residue contribution to protein stabilization

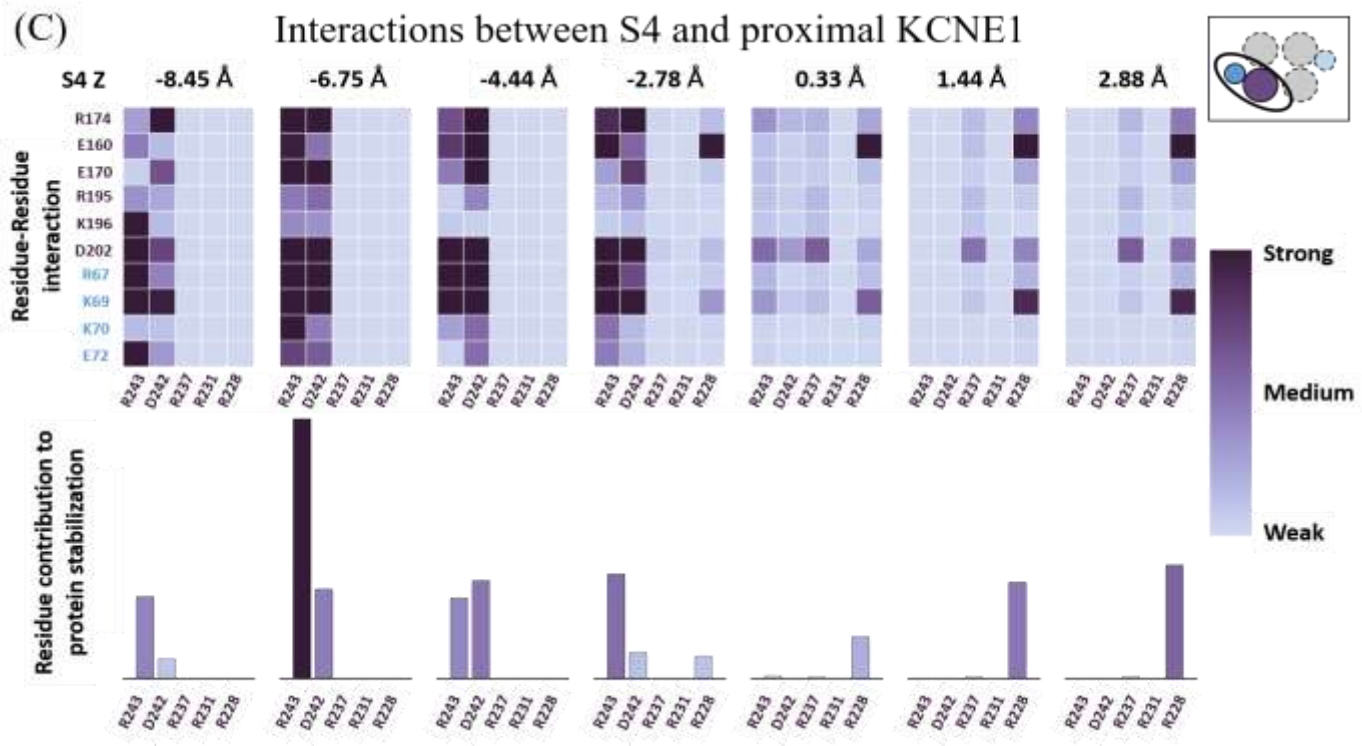

Figure S17. Residue-residue interactions that govern S4 movement in the Z direction at 60mV membrane voltage. ***A***: *Cartoon schema of important charged residues in a single KCNQ1 VSD and a corresponding KCNE1 transmembrane segment. These residues are used in the interaction energy calculations shown in panel B and C. Note that the S4 residues and the KCNE1 segment residues are identified in green (filled circles) and blue (empty circles), respectively. The top view of the KCNQ1 and KCNE1 segments is shown on the right and identically used in (B) and (C) to identify the S4-VSD (KCNQ1) and KCNE1 segments analyzed. The shaded circles with a continuous black outline represent the VSD (green) and KCNE1 (blue) of interest. This basic color scheme*

was used to distinguish S4 residues from other residues in the VSD of interest and also from the KCNE1 residues/segment. Note that the same KCNE1 residues are used in panels B and C energy calculations. ***B: S4 and distal KCNE1****. VSD and S4 residues used in this panel calculations are from the same KCNQ1 segment (identified by color in the inset; shaded pink with a continuous black outline.) The distal KCNE1 residues (inset, shaded blue with continuous black outline) were included in the calculations (the interacting segments are identified by a black oval). The top panel shows the strength of the interactions between S4 residues (pink, x-axis) with other residues within the VSD (pink, y-axis) and the KCNE1 segment (blue, y-axis). The residue-residue interactions were analyzed for different structures at different S4 Z positions (labeled on top of the respective panel) at 60mV membrane potential. The bottom panel shows the relative magnitude of each S4 residue contribution to protein stabilization (favorable interaction strength) corresponding to the top panel. The color-bar representing the strength of the interaction and the residue contribution to total protein energy is displayed on the right.* ***C: S4 and proximal KCNE1****. Similar calculations as in B, are performed with S4 residues and VSD (purple) proximal to the KCNE1 segment (blue); the interacting segments are identified with a black oval in the inset. Same format as panel B. (VSD, Voltage sensor domain)*

3.3: Additional Validation: Subconductances estimated directly from experiments (figure)

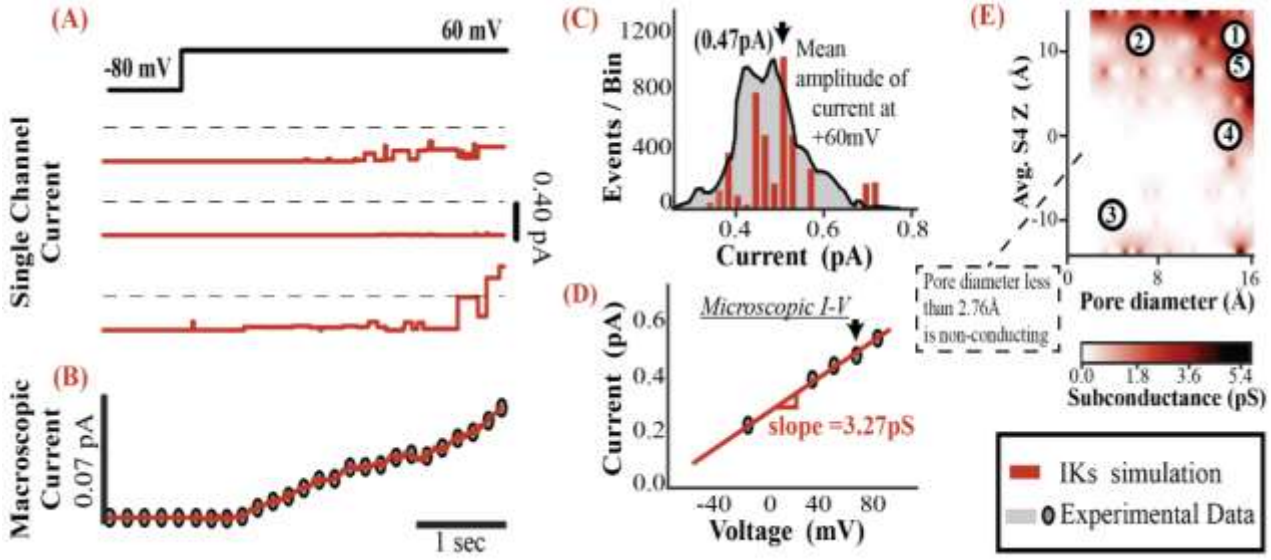

Figure S18. Model-based subconductance estimates using experimental data.

(A) Three of 100 simulated single-channel current traces for a step depolarizing voltage protocol from -80 to 60mV for 4 seconds. (B) The ensemble current (macroscopic, average of 100 traces) fits the experimental data (77) (C) Current amplitude histogram (red) of the simulated single-channel traces (at 60mV, mean amplitude of 0.47pA) and the corresponding experimental data (shaded grey,(77)). The arrow indicates the mean of the current amplitude histogram used in panel D at 60mV (similar arrow). Similar histograms are constructed for a range of V_m to obtain the microscopic I-V relationship in panel D. (D) The simulated mean current amplitude of single-channel traces for several V_m (red line) fits the experimental data (symbols) with a slope (mean conductance) =3.2pS as determined experimentally. (E) SC Map, estimated from purely

experimental data, projected onto two structural dimensions - PD and Avg.S4Z (77). The numbers refer to the structures in main text, Figure 2B. The legend for panels A-D is shown on the bottom right of the figure. Pore diameter less than 2.76Å (smaller than K^+ ion) is considered to be non-conducting. (pS, pico-Siemens (10e-12 Siemens)

References

1. Haitin, Y., R. Wiener, D. Shaham, A. Peretz, E.B.-T. Cohen, L. Shamgar, O. Pongs, J.A. Hirsch, and B. Attali. 2009. Intracellular domains interactions and gated motions of IKS potassium channel subunits. EMBO J. 28: 1994–2005.

2. Wiener, R., Y. Haitin, L. Shamgar, M.C. Fernández-Alonso, A. Martos, O. Chomsky-Hecht, G. Rivas, B. Attali, and J.A. Hirsch. 2008. The KCNQ1 (Kv7.1) COOH Terminus, a Multitiered Scaffold for Subunit Assembly and Protein Interaction. J. Biol. Chem. 283: 5815–5830.

3. Kang, C., C. Tian, F.D. Sönnichsen, J.A. Smith, J. Meiler, A.L. George, C.G. Vanoye, H.J. Kim, and C.R. Sanders. 2008. Structure of KCNE1 and Implications for How It Modulates the KCNQ1 Potassium Channel†‡. Biochemistry (Mosc.). 47: 7999–8006.

4. Du, L.-P., M.-Y. Li, K.-C. Tsai, Q.-D. You, and L. Xia. 2005. Characterization of binding site of closed-state KCNQ1 potassium channel by homology modeling, molecular docking, and pharmacophore identification. Biochem. Biophys. Res. Commun. 332: 677–687.

5. Van Horn, W.D., C.G. Vanoye, and C.R. Sanders. Working model for the structural basis for KCNE1 modulation of the KCNQ1 potassium channel. Curr. Opin. Struct. Biol. In Press, Corrected Proof.

6. Silva, J.R., H. Pan, D. Wu, A. Nekouzadeh, K.F. Decker, J. Cui, N.A. Baker, D. Sept, and Y. Rudy. 2009. A multiscale model linking ion-channel molecular dynamics and electrostatics to the cardiac action potential. Proc. Natl. Acad. Sci. 106: 11102–11106.

7. Nekouzadeh, A., and Y. Rudy. 2011. Continuum Molecular Simulation of Large Conformational Changes during Ion–Channel Gating. PLoS ONE. 6: e20186.

8. Long, S.B., X. Tao, E.B. Campbell, and R. MacKinnon. 2007. Atomic structure of a voltage-dependent K+ channel in a lipid membrane-like environment. Nature. 450: 376–382.

9. Yarov-Yarovoy, V., D. Baker, and W.A. Catterall. 2006. Voltage sensor conformations in the open and closed states in ROSETTA structural models of K(+) channels. Proc. Natl. Acad. Sci. U. S. A. 103: 7292–7297.

10. Rohl, C.A., C.E.M. Strauss, D. Chivian, and D. Baker. 2004. Modeling structurally variable regions in homologous proteins with rosetta. Proteins. 55: 656–677.

11. Sun, J., and R. MacKinnon. 2017. Cryo-EM Structure of a KCNQ1/CaM Complex Reveals Insights into Congenital Long QT Syndrome. Cell. 169: 1042-1050.e9.

12. Jespersen, T., M. Membrez, C.S. Nicolas, B. Pitard, O. Staub, S.-P. Olesen, I. Baró, and H. Abriel. 2007. The KCNQ1 potassium channel is down-regulated by ubiquitylating enzymes of the Nedd4/Nedd4-like family. Cardiovasc. Res. 74: 64–74.

13. Tian, C., C.G. Vanoye, C. Kang, R.C. Welch, H.J. Kim, A.L. George Jr, and C.R. Sanders. 2007. Preparation, functional characterization, and NMR studies of human KCNE1, a voltage-gated potassium channel accessory subunit associated with deafness and long QT syndrome. Biochemistry (Mosc.). 46: 11459–11472.

14. Sahu, I.D., B.M. Kroncke, R. Zhang, M.M. Dunagan, H.J. Smith, A. Craig, R.M. McCarrick, C.R. Sanders, and G.A. Lorigan. 2014. Structural investigation of the transmembrane domain of KCNE1 in proteoliposomes. Biochemistry (Mosc.). 53: 6392–6401.

15. Sahu, I.D., A.F. Craig, M.M. Dunagan, K.R. Troxel, R. Zhang, A.G. Meiberg, C.N. Harmon, R.M. McCarrick, B.M. Kroncke, C.R. Sanders, and G.A. Lorigan. 2015. Probing Structural Dynamics and Topology of the KCNE1 Membrane Protein in Lipid Bilayers via Site-Directed Spin Labeling and Electron Paramagnetic Resonance Spectroscopy. Biochemistry (Mosc.). 54: 6402–6412.

16. Zhang Rongfu, Sahu Indra D., Gibson Kaylee R., Muhammad Nefertiti B., Bali Avnika P., Comer Raven G., Liu Lishan, Craig Andrew F., Mccarrick Robert M., Dabney-Smith Carole, Sanders Charles R., and Lorigan Gary A. 2015. Development of electron spin echo envelope modulation spectroscopy to probe the secondary structure of recombinant membrane proteins in a lipid bilayer. Protein Sci. 24: 1707–1713.

17. Raveh, B., N. London, and O. Schueler-Furman. 2010. Sub-angstrom modeling of complexes between flexible peptides and globular proteins. Proteins. 78: 2029–2040.

18. Jalily Hasani, H., M. Ahmed, and K. Barakat. 2017. A comprehensive structural model for the human KCNQ1/KCNE1 ion channel. J. Mol. Graph. Model. 78: 26–47.

19. Sachyani, D., M. Dvir, R. Strulovich, G. Tria, W. Tobelaim, A. Peretz, O. Pongs, D. Svergun, B. Attali, and J.A. Hirsch. 2014. Structural Basis of a Kv7.1 Potassium Channel Gating Module: Studies of the Intracellular C-Terminal Domain in Complex with Calmodulin. Structure. 22: 1582–1594.

20. Shamgar, L., L. Ma, N. Schmitt, Y. Haitin, A. Peretz, R. Wiener, J. Hirsch, O. Pongs, and B. Attali. 2006. Calmodulin Is Essential for Cardiac IKS Channel Gating and Assembly: Impaired Function in Long-QT Mutations. Circ Res. 98: 1055–1063.

21. Chung, H.J. 2014. Role of calmodulin in neuronal Kv7/KCNQ potassium channels and epilepsy. Front. Biol. : 1–11.

22. Gamper, N., Y. Li, and M.S. Shapiro. 2005. Structural Requirements for Differential Sensitivity of KCNQ K+ Channels to Modulation by Ca2+/Calmodulin. Mol Biol Cell. 16: 3538–3551.

23. Touw, W.G., C. Baakman, J. Black, T.A.H. te Beek, E. Krieger, R.P. Joosten, and G. Vriend. 2015. A series of PDB-related databanks for everyday needs. Nucleic Acids Res. 43: D364–D368.

24. Kabsch, W., and C. Sander. 1983. Dictionary of protein secondary structure: pattern recognition of hydrogen-bonded and geometrical features. Biopolymers. 22: 2577–2637.

25. Haitin, Y., and B. Attali. 2008. The C-terminus of Kv7 channels: a multifunctional module. J. Physiol. 586: 1803–1810.

26. Kaufmann, K.W., G.H. Lemmon, S.L. DeLuca, J.H. Sheehan, and J. Meiler. 2010. Practically Useful: What the Rosetta Protein Modeling Suite Can Do for You. Biochemistry (Mosc.). 49: 2987–2998.

27. Chen, J., R. Zheng, Y.F. Melman, and T.V. McDonald. Functional Interactions between KCNE1 C-Terminus and the KCNQ1 Channel. PLoS ONE. 4: e5143.

28. Raveh, B., N. London, L. Zimmerman, and O. Schueler-Furman. 2011. Rosetta FlexPepDock ab-initio: Simultaneous Folding, Docking and Refinement of Peptides onto Their Receptors. PLoS ONE. 6: e18934.

29. Webb, B., and A. Sali. 2014. Protein structure modeling with MODELLER. Methods Mol. Biol. Clifton NJ. 1137: 1–15.

30. Nakajo, K., M.H. Ulbrich, Y. Kubo, and E.Y. Isacoff. 2010. Stoichiometry of the KCNQ1 - KCNE1 ion channel complex. Proc. Natl. Acad. Sci. 107: 18862–18867.

31. Nakajo, K., M.H. Ulbrich, Y. Kubo, and E.Y. Isacoff. 2010. Stoichiometry of KCNQ1-KCNE1 Ion Channel Complex is Flexible and Density-Dependent. Biophys. J. 98: 136a-137a.

32. Wang, K., C. Terrenoire, K.J. Sampson, V. Iyer, J.D. Osteen, J. Lu, G. Keller, D.N. Kotton, and R.S. Kass. 2011. Biophysical properties of slow potassium channels in human embryonic stem cell derived cardiomyocytes implicate subunit stoichiometry. J. Physiol. 589: 6093–6104.

33. Yu, H., Z. Lin, M.E. Mattmann, B. Zou, C. Terrenoire, H. Zhang, M. Wu, O.B. McManus, R.S. Kass, C.W. Lindsley, C.R. Hopkins, and M. Li. 2013. Dynamic subunit stoichiometry confers a progressive continuum of pharmacological sensitivity by KCNQ potassium channels. Proc. Natl. Acad. Sci. 110: 8732-8737.

34. Murray, C.I., M. Westhoff, J. Eldstrom, E. Thompson, R. Emes, and D. Fedida. 2016. Unnatural amino acid photo-crosslinking of the IKs channel complex demonstrates a KCNE1:KCNQ1 stoichiometry of up to 4:4. eLife. : e11815.

35. Baker, O.S., H.P. Larsson, L.M. Mannuzzu, and E.Y. Isacoff. 1998. Three Transmembrane Conformations and Sequence-Dependent Displacement of the S4 Domain in Shaker K+ Channel Gating. Neuron. 20: 1283–1294.

36. Ruta, V., J. Chen, and R. MacKinnon. 2005. Calibrated Measurement of Gating-Charge Arginine Displacement in the KvAP Voltage-Dependent K+ Channel. Cell. 123: 463–475.

37. Posson, D.J., P. Ge, C. Miller, F. Bezanilla, and P.R. Selvin. 2005. Small vertical movement of a K+ channel voltage sensor measured with luminescence energy transfer. Nature. 436: 848–851.

38. Long, S.B., E.B. Campbell, and R. MacKinnon. 2005. Crystal Structure of a Mammalian Voltage-Dependent Shaker Family K+ Channel. Science. 309: 897–903.

39. Tombola, F., M.M. Pathak, and E.Y. Isacoff. 2006. How Does Voltage Open an Ion Channel? Annu. Rev. Cell Dev. Biol. 22: 23–52.

40. Kalstrup, T., and R. Blunck. 2016. Probing the S4-S5 Linker Movement During Activation in KV Channels. Biophys. J. 110: 104a.

41. Börjesson, S.I., and F. Elinder. 2008. Structure, Function, and Modification of the Voltage Sensor in Voltage-Gated Ion Channels. Cell Biochem. Biophys. 52: 149–174.

42. Haitin, Y., I. Yisharel, E. Malka, L. Shamgar, H. Schottelndreier, A. Peretz, Y. Paas, and B. Attali. 2008. S1 Constrains S4 in the Voltage Sensor Domain of Kv7.1 K+ Channels. PLOS ONE. 3: e1935.

43. Rocheleau, J.M., and W.R. Kobertz. 2008. KCNE Peptides Differently Affect Voltage Sensor Equilibrium and Equilibration Rates in KCNQ1 K+ Channels. J. Gen. Physiol. 131: 59–68.

44. Lvov, A., S.D. Gage, V.M. Berrios, and W.R. Kobertz. 2010. Identification of a protein–protein interaction between KCNE1 and the activation gate machinery of KCNQ1. J. Gen. Physiol. 135: 607–618.

45. Wu, D., K. Delaloye, M.A. Zaydman, A. Nekouzadeh, Y. Rudy, and J. Cui. 2010. State-dependent electrostatic interactions of S4 arginines with E1 in S2 during Kv7.1 activation. J. Gen. Physiol. 135: 595–606.

46. Ma, L.-J., I. Ohmert, and V. Vardanyan. 2011. Allosteric Features of KCNQ1 Gating Revealed by Alanine Scanning Mutagenesis. Biophys. J. 100: 885–894.

47. Ruscic, K.J., F. Miceli, C.A. Villalba-Galea, H. Dai, Y. Mishina, F. Bezanilla, and S.A.N. Goldstein. 2013. IKs channels open slowly because KCNE1 accessory subunits slow the movement of S4 voltage sensors in KCNQ1 pore-forming subunits. Proc. Natl. Acad. Sci. 110: E559–E566.

48. Eckey, K., E. Wrobel, G. Seebohm, L. Pott, N. Schmitt, and N. Strutz-Seebohm. 2014. Novel Kv7.1-phosphatidylinositol 4,5-bisphosphate (PIP2) interaction sites uncovered by charge neutralization scanning. J. Biol. Chem. : jbc.M114.589796.

49. Kleiger, G., A. Saha, S. Lewis, B. Kuhlman, and R.J. Deshaies. 2009. Rapid E2-E3 assembly and disassembly enable processive ubiquitylation of cullin-RING ubiquitin ligase substrates. Cell. 139: 957–968.

50. Callenberg, K.M., O.P. Choudhary, G.L. de Forest, D.W. Gohara, N.A. Baker, and M. Grabe. 2010. APBSmem: A Graphical Interface for Electrostatic Calculations at the Membrane. PLoS ONE. 5: e12722.

51. Dolinsky, T.J., J.E. Nielsen, J.A. McCammon, and N.A. Baker. 2004. PDB2PQR: an automated pipeline for the setup of Poisson–Boltzmann electrostatics calculations. Nucleic Acids Res. 32: W665–W667.

52. Dolinsky, T.J., P. Czodrowski, H. Li, J.E. Nielsen, J.H. Jensen, G. Klebe, and N.A. Baker. 2007. PDB2PQR: expanding and upgrading automated preparation of biomolecular structures for molecular simulations. Nucleic Acids Res. 35: W522–W525.

53. Bank, R., and M. Holst. 2003. A New Paradigm for Parallel Adaptive Meshing Algorithms. SIAM Rev. 45: 291–323.

54. Holst, M. 2001. Adaptive Numerical Treatment of Elliptic Systems on Manifolds. Adv. Comput. Math. 15: 139–191.

55. Prusinkiewicz, P., and A. Lindenmayer. 1990. The algorithmic beauty of plants. New York: Springer-Verlag.

56. Jaillet, L., A. Yershova, S.M. La Valle, and T. Siméon. 2005. Adaptive tuning of the sampling domain for dynamic-domain RRTs. In: 2005 IEEE/RSJ International Conference on Intelligent Robots and Systems. IEEE. pp. 2851–2856.

57. Yershova, A., and S.M. LaValle. 2007. Improving motion-planning algorithms by efficient nearest-neighbor searching. IEEE Trans. Robot. 23: 151–157.

58. Zhong, J., and J. Su. 2012. Triple-Rrts for robot path planning based on narrow passage identification. In: 2012 International Conference on Computer Science and Information Processing (CSIP). pp. 188–192.

59. Yershova, A., and S.M. LaValle. 2009. Motion Planning for Highly Constrained Spaces. In: Robot Motion and Control 2009. Springer, London. pp. 297–306.

60. Nekouzadeh, A., and Y. Rudy. 2016. Conformational changes of an ion-channel during gating and emerging electrophysiologic properties: Application of a computational approach to cardiac Kv7.1. Prog. Biophys. Mol. Biol. 120: 18–27.

61. Broomand, A., and F. Elinder. 2008. Large-Scale Movement within the Voltage-Sensor Paddle of a Potassium Channel—Support for a Helical-Screw Motion. Neuron. 59: 770–777.

62. Jiang, Y., V. Ruta, J. Chen, A. Lee, and R. MacKinnon. 2003. The principle of gating charge movement in a voltage-dependent K+ channel. Nature. 423: 42–48.

63. Hackos, D.H., T.-H. Chang, and K.J. Swartz. 2002. Scanning the Intracellular S6 Activation Gate in the Shaker K+ Channel. J. Gen. Physiol. 119: 521–531.

64. Phillips James C., Braun Rosemary, Wang Wei, Gumbart James, Tajkhorshid Emad, Villa Elizabeth, Chipot Christophe, Skeel Robert D., Kalé Laxmikant, and Schulten Klaus. 2005. Scalable molecular dynamics with NAMD. J. Comput. Chem. 26: 1781–1802.

65. Humphrey, W., A. Dalke, and K. Schulten. 1996. VMD: visual molecular dynamics. J. Mol. Graph. 14: 33–38, 27–28.

66. Huang, J., S. Rauscher, G. Nawrocki, T. Ran, M. Feig, B.L. de Groot, H. Grubmüller, and A.D. MacKerell Jr. 2017. CHARMM36m: an improved force field for folded and intrinsically disordered proteins. Nat. Methods. 14: 71–73.

67. Baker, N.A., D. Sept, S. Joseph, M.J. Holst, and J.A. McCammon. 2001. Electrostatics of nanosystems: Application to microtubules and the ribosome. Proc. Natl. Acad. Sci. 98: 10037–10041.

68. Breiman, L. 2001. Random Forests. Mach. Learn. 45: 5–32.

69. Buitinck, L., G. Louppe, M. Blondel, F. Pedregosa, A. Mueller, O. Grisel, V. Niculae, P. Prettenhofer, A. Gramfort, J. Grobler, R. Layton, J. Vanderplas, A. Joly, B. Holt, and G. Varoquaux. 2013. API design for machine learning software: experiences from the scikit-learn project. ArXiv13090238 Cs. .

70. Pedregosa, F., G. Varoquaux, A. Gramfort, V. Michel, B. Thirion, O. Grisel, M. Blondel, P. Prettenhofer, R. Weiss, V. Dubourg, J. Vanderplas, A. Passos, D. Cournapeau, M. Brucher, M. Perrot, and É. Duchesnay. 2011. Scikit-learn: Machine Learning in Python. J. Mach. Learn. Res. 12: 2825–2830.

71. Tipping, M.E., and C.M. Bishop. 1999. Probabilistic Principal Component Analysis. J. R. Stat. Soc. Ser. B Stat. Methodol. 61: 611–622.

72. Halko, N., P. Martinsson, and J. Tropp. 2011. Finding Structure with Randomness: Probabilistic Algorithms for Constructing Approximate Matrix Decompositions. SIAM Rev. 53: 217–288.

73. Weiss, Y., and E.H. Adelson. 1995. MIT Media Laboratory Perceptual Computing Section Technical Report No. 344 Motion Estimation and Segmentation Using a Recurrent Mixture of Experts Architecture. In: IEEE Workshop on Neural Network for Signal Processing. Citeseer.

74. Hastings, W.K. 1970. Monte Carlo sampling methods using Markov chains and their applications. Biometrika. 57: 97–109.

75. Gilks, W.R., S. Richardson, and D. Spiegelhalter. 1995. Markov Chain Monte Carlo in Practice. CRC Press.

76. Scherer, M.K., B. Trendelkamp-Schroer, F. Paul, G. Pérez-Hernández, M. Hoffmann, N. Plattner, C. Wehmeyer, J.-H. Prinz, and F. Noé. 2015. PyEMMA 2: A Software Package

for Estimation, Validation, and Analysis of Markov Models. J. Chem. Theory Comput. 11: 5525–5542.

77. Werry, D., J. Eldstrom, Z. Wang, and D. Fedida. 2013. Single-channel basis for the slow activation of the repolarizing cardiac potassium current, IKs. Proc. Natl. Acad. Sci. 110: E996–E1005.

Additional References

Moss AJ, Kass RS (2005) Long QT syndrome: from channels to cardiac arrhythmias. J Clin Invest 115(8):2018–2024.

Chouabe C, et al. (2000) Novel mutations in KvLQT1 that affect Iks activation through interactions with Isk. Cardiovasc Res 45(4):971–980.

Goldman AM, et al. (2009) Arrhythmia in Heart and Brain: KCNQ1 Mutations Link Epilepsy and Sudden Unexplained Death. Sci Transl Med 1(2):2ra6.

Lopez GA, Nung Jan Y, Jan LY (1994) Evidence that the S6 segment of the Shaker voltage-gated K+ channel comprises part of the pore. Nature 367(6459):179–182.

Ding S, Horn R (2002) Tail End of the S6 Segment. J Gen Physiol 120(1):87–97.

Lane TJ, Shukla D, Beauchamp KA, Pande VS (2013) To Milliseconds and Beyond: Challenges in the Simulation of Protein Folding. Curr Opin Struct Biol 23(1):58–65.

Breiman L (2001) Random Forests. Mach Learn 45(1):5–32.

Chapman ML, VanDongen AMJ (2005) K channel subconductance levels result from heteromeric pore conformations. J Gen Physiol 126(2):87–103.

Chapman ML, VanDongen HMA, VanDongen AMJ (1997) Activation-Dependent Subconductance Levels in the drk1 K Channel Suggest a Subunit Basis for Ion Permeation and Gating. Biophys J 72(2):708–719.

Cheneke BR, van den Berg B, Movileanu L (2011) Analysis of Gating Transitions among the Three Major Open States of the OpdK Channel. Biochemistry (Mosc) 50(22):4987–4997.

Zifarelli G, Pusch M (2007) CLC chloride channels and transporters: a biophysical and physiological perspective. Reviews of Physiology, Biochemistry and

Pharmacology, ed Amara SG (Springer Berlin Heidelberg, Berlin, Heidelberg), pp 23–76.

Shieh CC, Kirsch GE (1994) Mutational analysis of ion conduction and drug binding sites in the inner mouth of voltage-gated K+ channels. Biophysical Journal 67(6):2316–2325.

Bezanilla F (2005) The Origin of Subconductance Levels in Voltage-gated K+ Channels. J Gen Physiol 126(2):83–86.

Ruscic KJ, et al. (2013) IKs channels open slowly because KCNE1 accessory subunits slow the movement of S4 voltage sensors in KCNQ1 pore-forming subunits. Proc Natl Acad Sci 110(7):E559–E566.

Nakajo K, Kubo Y (2014) Steric hindrance between S4 and S5 of the KCNQ1/KCNE1 channel hampers pore opening. Nat Commun 5. doi:10.1038/ncomms5100.

Gagnon DG, Bezanilla F (2010) The contribution of individual subunits to the coupling of the voltage sensor to pore opening in Shaker K channels: effect of ILT mutations in heterotetramers. J Gen Physiol 136(5):555–568.

Horn R, Ding S, Gruber HJ (2000) Immobilizing the moving parts of voltage-gated ion channels. J Gen Physiol 116(3):461–476.

Ledwell JL, Aldrich RW (1999) Mutations in the S4 region isolate the final voltage-dependent cooperative step in potassium channel activation. J Gen Physiol 113(3):389–414.

Pathak M, Kurtz L, Tombola F, Isacoff E (2005) The Cooperative Voltage Sensor Motion that Gates a Potassium Channel. J Gen Physiol 125(1):57–69.

Yifrach O, Zandany N, Shem-Ad T (2009) Examining cooperative gating phenomena in voltage-dependent potassium channels: taking the energetic approach. Methods Enzymol 466:179–209.

Zagotta WN, Hoshi T, Aldrich RW (1994) Shaker potassium channel gating. III: Evaluation of kinetic models for activation. J Gen Physiol 103(2):321–362.

Gilks WR, Richardson S, Spiegelhalter D (1995) Markov Chain Monte Carlo in Practice (CRC Press).

Brest J, Zumer V, Maucec MS (2006) Self-Adaptive Differential Evolution Algorithm in Constrained Real-Parameter Optimization. 2006 IEEE International Conference on Evolutionary Computation, pp 215–222.